

Ultra-Sharp Nanowire Arrays Natively Permeate, Record, and Stimulate Intracellular Activity in Neuronal and Cardiac Networks

Ren Liu, Jihwan Lee, Youngbin Tchoe, Deborah Pre, Andrew M. Bourhis, Agnieszka D'Antonio-Chronowska, Gaelle Robin, Sang Heon Lee, Yun Goo Ro, Ritwik Vatsyayan, Karen J. Tonsfeldt, Lorraine A. Hossain, M. Lisa Phipps, Jinkyong Yoo, John Nogan, Jennifer S. Martinez, Kelly A. Frazer, Anne G. Bang, and Shadi A. Dayeh*

Intracellular access with high spatiotemporal resolution can enhance the understanding of how neurons or cardiomyocytes regulate and orchestrate network activity and how this activity can be affected with pharmacology or other interventional modalities. Nanoscale devices often employ electroporation to transiently permeate the cell membrane and record intracellular potentials, which tend to decrease rapidly with time. Here, one reports innovative scalable, vertical, ultrasharp nanowire arrays that are individually addressable to enable long-term, native recordings of intracellular potentials. One reports electrophysiological recordings that are indicative of intracellular access from 3D tissue-like networks of neurons and cardiomyocytes across recording days and that do not decrease to extracellular amplitudes for the duration of the recording of several minutes. The findings are validated with cross-sectional microscopy, pharmacology, and electrical interventions. The experiments and simulations demonstrate that the individual electrical addressability of nanowires is necessary for high-fidelity intracellular electrophysiological recordings. This study advances the understanding of and control over high-quality multichannel intracellular recordings and paves the way toward predictive, high-throughput, and low-cost electrophysiological drug screening platforms.

1. Introduction

Reliable intracellular electrophysiological access of neurons is essential to properly measure and interrogate the ionic conductances that underscore neuronal activity. The gold standard technique for intracellular recordings is whole-cell patch clamp electrophysiology, which has revolutionized our understanding of the neuronal dynamics of individual excitable cells. A typical patch clamp recording trace^[1] and simplified circuit model of the patch pipette-neuron interface shown in Figure 1a, where high coupling coefficient and large dynamic range are observed through leak-tight, Giga-ohm seal interface between the pipette and the cell membrane. In patch clamp electrophysiology, access to the intracellular currents and potentials are obtained at the cost of the health of the cell; most intracellular recordings obtained with patch clamp are extremely labor intensive and provide

R. Liu, J. Lee, Y. Tchoe, A. M. Bourhis, S. H. Lee, Y. G. Ro, R. Vatsyayan, K. J. Tonsfeldt, L. A. Hossain, S. A. Dayeh
Integrated Electronics and Biointerfaces Laboratory
Department of Electrical and Computer Engineering
University of California San Diego
9500 Gilman Drive, La Jolla, CA 92093, USA
E-mail: sdayeh@eng.ucsd.edu

D. Pre, G. Robin, A. G. Bang
Conrad Prebys Center for Chemical Genomics
Sanford Burnham Prebys Medical Discovery Institute
10901 North Torrey Pines Road, La Jolla, CA 92037, USA

A. D'Antonio-Chronowska, K. A. Frazer
Department of Pediatrics
University of California San Diego
9500 Gilman Drive, La Jolla, CA 92093, USA

 The ORCID identification number(s) for the author(s) of this article can be found under <https://doi.org/10.1002/adfm.202108378>.

K. J. Tonsfeldt
Center for Reproductive Science and Medicine
Department of Obstetrics, Gynecology, and Reproductive Sciences
University of California San Diego
9500 Gilman Drive, La Jolla, CA 92093, USA

M. L. Phipps, J. Yoo
Center for Integrated Nanotechnologies
Los Alamos National Laboratory
Los Alamos, NM 87545, USA

J. Nogan
Center for Integrated Nanotechnologies
Sandia National Laboratories
Albuquerque, NM 87185, USA

J. S. Martinez
Center for Materials Interfaces in Research and Applications
and Department of Applied Physics and Materials Science
Northern Arizona University
624 S. Knoles Dr. Flagstaff, Flagstaff, AZ 86011, USA

DOI: 10.1002/adfm.202108378

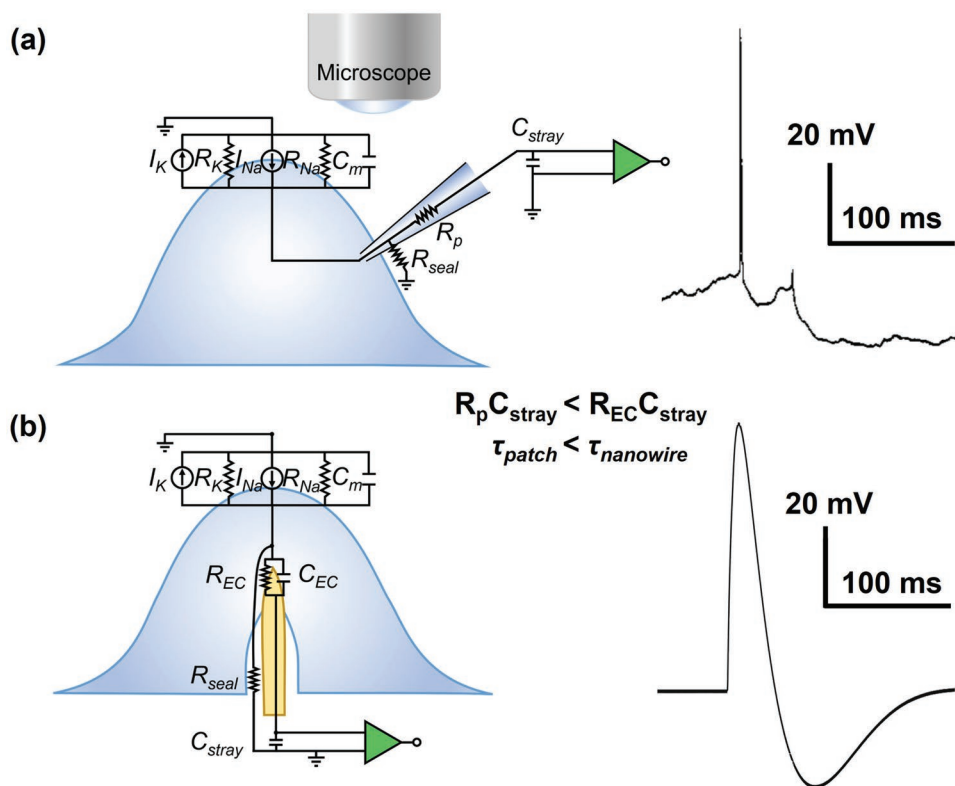


Figure 1. a) Simplified circuit model and typical recording segment from patch clamp electrode–neuron interface from in vivo cat neocortical neurons. Reprinted with permission from Steriade et al. *J. Neurophys.* 2001, 85, 1969. b) Simplified circuit model and an example recording segment observed from mouse hippocampal neurons at 13 DIV for NW electrode–neuron interface with TDT system.

less than 30–60 min of data.^[2–4] Instead, evolving technological advances include vertical, nanoscale interface electrodes which are widely utilized to allow intracellular access and recording, with varied structures and interface coupling strategies such as membrane penetration, engulfment, electroporation, and optoporation.^[5–17] These techniques can scale intracellular electrophysiological recordings to a large number of cells in extended networks with high spatial resolution. Additionally, due to their nanoscale size, they are minimally destructive and are envisioned to extend the recording duration for days to weeks, all while maintaining the high sensitivity comparable to that of patch clamp recordings. However, most state-of-the-art vertical nanoelectrodes are required to actively deliver electroporation currents to temporarily and destructively permeate neuronal membranes to have intracellular access. Unfortunately, that process is also accompanied with large, irreversible micrometer-scale gas bubble formations^[5–7] due to water electrolysis at the surface of the high-impedance nanoelectrodes.

One successful example of the vertical electrode type is the μm -scale gold mushroom-shaped microelectrode pillar arrays. The gold mushroom arrays demonstrated intracellular “in-cell” recordings with proper engulfment of the electrodes by the target cell membrane with a short electroporation pulse.^[7] Xie et al.^[8] similarly utilized electroporation with their sub-100 nm, 4×4 platinum nanopillar pad arrays to achieve intracellular action potential (AP) recordings that yielded maximum potentials of 11.8 mV postelectroporation, but which eventually attenuated to 30% of the initial amplitude after 2 min and to

1% after 10 min reaching an extracellular potential of 200 μV . Abbott et al.^[10] attained intracellular recordings by electroporation from arrays composed of 4096 sites built atop complementary metal-oxide semiconductor (CMOS) acquisition electronics. Each electrode contact was composed of nine nanowires coated with low-impedance platinum-black which reduced bubble formation during electroporation. To eliminate the often-uncontrolled destructive process of electroporation, others have used nanowires to mechanically puncture the cell membrane to achieve intracellular recordings.^[9,16–17] Zhao et al.^[17] gained intracellular access with their nanowire field-effect transistor into both neuron and cardiomyocytes in culture by probing the cells with an U-shaped 15 nm diameter Si nanowire. Other nanostructures than 1D nanowires have also been investigated for intracellular recordings. Desbiolles et al.^[11] achieved passive intracellular recording with their novel 3D nanovolcano structure comprising of sub-20 nm nanoring. The aforementioned advances have demonstrated intracellular recordings with either cardiomyocyte cells or neurons. Neuronal recording is more challenging because unlike cardiomyocytes, most neurons do not have regular, periodic firing, and also have interspersed axons that result in different waveform and potential dynamics based on the electrode and cell interface locations.^[13] Furthermore, neurons possess relatively softer elastic characteristics and lower stiffness that require more contact forces to penetrate their membranes.^[18,19] Of the vertical nanoelectrodes, ultrasharp nanowires (USNWs) hold the most promise for recording intracellular potentials^[20–25] and subthreshold synaptic potentials.^[26]

Generally, decreasing the NW tip diameter and increasing the NW height allows easier intracellular access via penetration.^[19,27,28] Using Si NWs with tip diameters as small as 60 nm, we recorded in vitro from mouse hippocampal neurons APs with amplitudes up to 99 mV in AP, a similar magnitude to that recorded with patch clamp, and with subthreshold sensitivity.^[26] These potentials were recorded with a Tucker-Davis Technologies (TDT) electrophysiological recording system using their MZ60 microelectrode array (MEA) interface with vertical NW array platform.^[26] Using the same recording system with our USNWs subject of this work and the same mouse hippocampal neurons, we have also recorded APs with peak-to-peak amplitudes of 106 mV (Figure 1b). As illustrated in Figure 1b and further discussed in this work, APs recorded with NWs exhibit temporal broadening compared to APs recorded with patch-clamp due to increased time constants that arise from parasitic capacitances and large electrochemical interfacial impedance between the NW electrode and the intracellular medium, consistent with prior results.^[6,17,26] To obtain reliable recordings from USNW arrays, we used a recording setup we have successfully implemented in recording electrophysiological activity from intact brains in birds,^[29,30] rodents,^[30–32] non-human primates,^[30] and humans.^[33–37] The maximum potentials that can be recorded with this setup using amplifiers from Intan Technologies LLC is ± 6.4 mV. Therefore, the recorded action potentials for most of the measurements reported in this work are truncated at 6.4 mV. Despite these instrumental shortcomings, we demonstrate that USNWs yield higher fidelity in intracellular recordings from neurons and cardiomyocytes than any prior nanoscale devices and illustrate with experiments and modeling that individual electrical addressability is an essential precursor for obtaining a large dynamic range in these recordings, a design flaw in prior work that used nanowires to interface with neurons and cardiomyocytes.

2. Results and Discussion

We demonstrate a scalable, silicon-based USNW array interface system that natively permeates cell membranes and records intracellular APs from cultured rat cortical neurons and from induced pluripotent stem cell (iPSC)-derived cardiovascular progenitor cells (iPSC-CVPCs). Critically, these intracellular recordings are achievable without electroporation. Each contact is composed of a small footprint metallic pad with a diameter of 2 μm , addressing an individual USNW electrode. We observed significantly higher peak-to-peak signal amplitude from recordings with a single USNW compared to those from multiple USNWs, demonstrating the importance of independent electrical addressability for recording high amplitude intracellular potentials.^[26] Using sequential focused ion beam (FIB) sectioning to reveal the NW–neuron interface, we assessed the relative position of our metal-coated USNW tips with diameters in the range of 30–70 nm with respect to the neuronal cells. Significantly, we detected graded membrane potentials prior to the recorded APs from 3D multilayered “tissue” like neuronal networks, justifying the innate ability of our USNWs to record subthreshold potentials, and pharmacologically modulated network activities. Our recordings were not affected by the

maturation of the primary culture and glial proliferation, as we achieved high-quality recordings from cultured primary rat cortical neurons up to 19 d in vitro (DIV). We also observed clear AP propagation in cardiac networks that can be interrogated by electrical stimulation. Our USNW platform development and their remaining limitations are discussed in detail, uncovering the promise of USNW–neuron interfaces and the challenges set forth to fulfill their full potential.

2.1. Fabrication of USNW Arrays

To achieve sub-10 nm vertical USNW arrays, we employed successive and selective oxidation and etching of top-down etched Si USNWs on a Si substrate, invoking standard integrated circuit fabrication technologies in innovative combinations. **Figure 2** and Figures S1–S6 (Supporting Information) exhibit details of the fabrication process. Our process involves the dry etching of Si USNW arrays followed by selective oxidation and oxide etching to thin down the NW tips, and the electron-beam lithography and photolithography to attain individually addressable USNW arrays as illustrated in the process schematics (Figure S1, Supporting Information). Achieving sub-10 nm diameter USNW tips involves multiple selective oxidations and oxide stripping steps (Figure 2b–f), which yield a fully oxidized Si NW with a smooth surface morphology (Figure 2g). Typical cycles of oxidation and stripping include 10 min–2 h of thermal oxidation at 1100 °C and 10 s–2 min of buffered oxide etch. To achieve electrical insulation in between individual USNWs, a final oxidation step is used to fully react with the Si NW and the surface of the substrate. The resulting SiO₂ USNW is then selectively coated with a Pt metal layer (Figure S3, Supporting Information) and a blanket plasma-enhanced chemical vapor deposition (PECVD) step is used to deposit 500 nm thick SiO₂ passivation layer above the metal leads which is then selectively etched to expose the NW tip (Figure 2b and Figure S4, Supporting Information).

Our first set of devices with 300 nm PECVD deposited SiO₂ layer was not sufficient to passivate and prevent the delamination of the 10 nm Cr/100 nm Au metal interconnects in in vitro cell culture after 14 d (Figure S5a–c, Supporting Information). We added a 10 nm thin Ti layer atop the Cr/Au metal leads to promote the adhesion between the thinly formed TiO₂ layer and the PECVD deposited SiO₂ layer on top of the 10 nm Ti layer, and increased the thickness of the SiO₂ layer to 500 nm. Accelerated aging experiments by submerging the device into the saline solution at 60 °C for 3 d, equivalent of 15 d at 37 °C, demonstrated the robustness of the platform against delamination (Figure S5d,e, Supporting Information).

Deposited PECVD oxide layers that had a root-mean-square (rms) surface roughness of less than one nm were too smooth to promote neuronal cell culture adhesion even under the presence of adhesion promoters such as PEI or Matrigel.^[38,39] We calibrated the surface roughness of SiO₂ (thermally grown and PECVD deposited, Figure S6, Supporting Information), and found that the rough surface with rms roughness of 2–5 nm promotes the cell adhesion according to our initial cell culture experiments. In addition to the SiO₂ passivation, we added a 500 nm thick parylene C layer and roughened

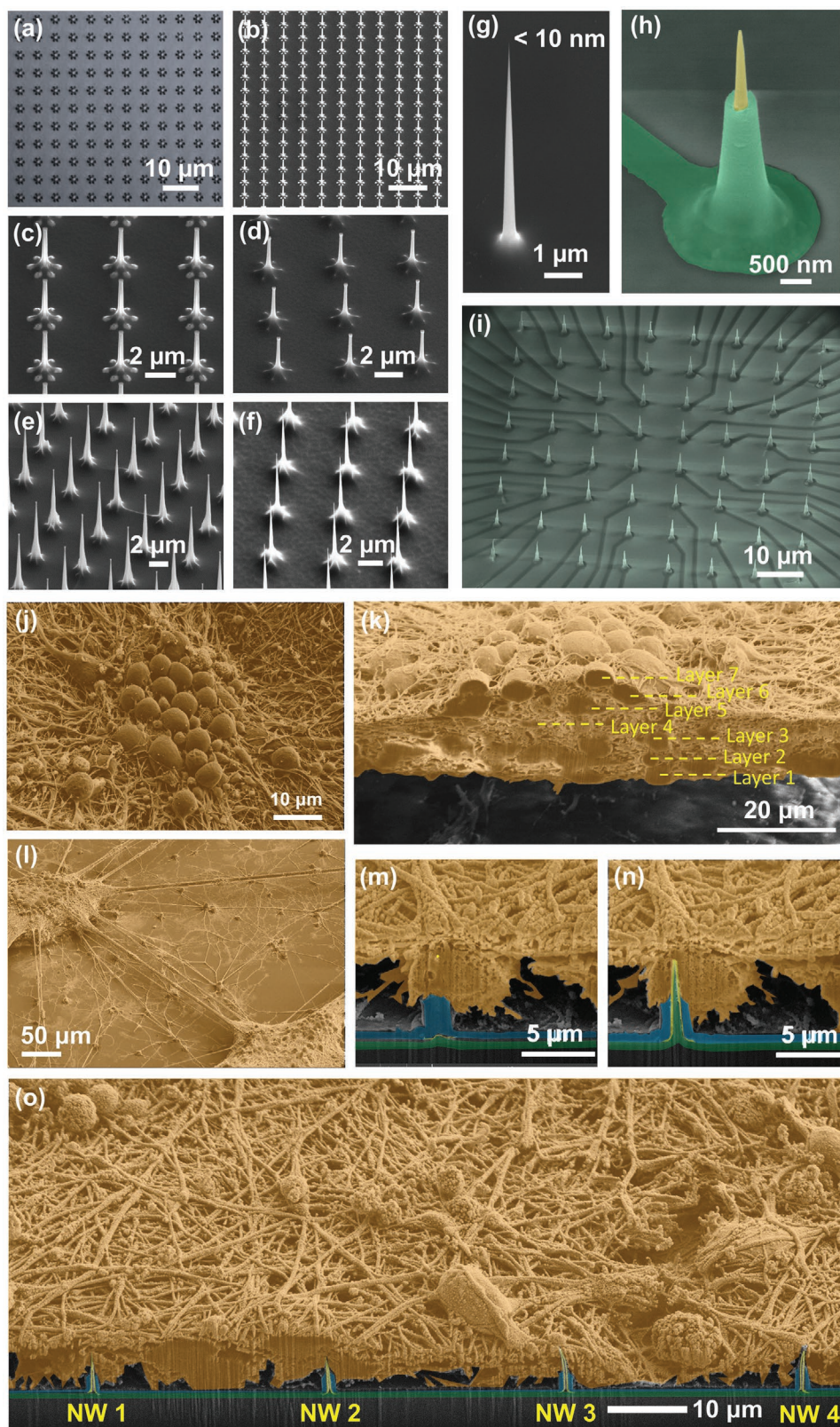


Figure 2. Si USNW array fabrication and characterization of structure and the electrode–neural interface. Overview of the fabrication process. a) Top-view optical microscope image of patterned Ni dot arrays for Si nanowire etching. The center dot diameter was 800 nm. The peripheral dot diameter was 300 nm. b–d) Example SEM images that shows sequential oxidation and oxide stripping leading to reduced diameter of the NWs in the array, smoothing of the NW surface and the tapered structure. e, f) Example SEM images that show dry etching, sequential oxidation, and oxide stripping

its surface with O₂ plasma treatment (Figure S7, Supporting Information; rms roughness of 7 nm), resulting in better cell viability in comparison to the bare SiO₂ surface. The mechanism for this increased cell viability is thought to arise from the inherent nanoscale surface roughness of parylene C and its stable hydrophilic surface for cell adherence after plasma treatment.^[40]

Devices passivated with additional parylene C coating were used in our experiments. A picture of the overall packaged device is shown in Figure S8 (Supporting Information). The optimized surface materials and roughness were found to help neurite growth (Figure S12, Supporting Information) and neuronal and cardiac network formation on the USNW array platform (Figures S13–S17, Supporting Information).

Figure 2j shows representative top-view scanning electron microscope (SEM) images of the cultured rat cortical neurons on the surface of our devices. We observed the formation of continuous layers (Figure S14a,b, Supporting Information) and of satellite neuronal clusters (Figure S14c,d, Supporting Information). FIB sectioning revealed that the cultured neurons exhibit multilayer structure (Figure 2k and Figure S15, Supporting Information: noncolorized SEM image) with extensive neurite connection that suggest excellent cell viability on parylene C-coated vertical USNW arrays. FIB-sectioning in the USNW array region illustrated that the USNW tip resides inside the neuron soma as shown in the time-sequenced SEM images (Figure 2m–o and Figure S16, Supporting Information: noncolorized SEM images). While the resolution of these SEM images does not conclusively rule out that the USNW is indeed inside the soma, these images coupled with the recorded and relatively significant intracellular potentials support our hypothesis of intracellular access.

As fabricated, the USNWs exhibit impedances exceeding 10 MΩ at 1 kHz (Figure S9, Supporting Information) that limit a stimulation current to several nanoamperes to avoid electrolyzing water (Figure S11a,c, Supporting Information). However, in silent or moderately active recording, we do not know a priori which USNWs are capable of intracellular stimulation. To enable extracellular current stimulation at the periphery of the USNW array, we selectively coated poly(3,4-ethylenedioxythiophene):poly(styrenesulfonate) (PEDOT:PSS) on selected USNWs (Figure S10, Supporting Information) which reduced the electrode impedance by ≈50× and enabled microampere levels of current to stimulate without causing water electrolysis (Figure S11b,d, Supporting Information). However, for all recordings in this manuscript, we did not use the PEDOT:PSS for stimulation. We stimulated USNWs located at the periphery of the USNW array for 20 to 40 cycles of 10 nA, 500 μs current pulses injected by a 128-channel Intan RHS2000 stimulation controller and subsequently recorded the electrophysiological activity with the USNWs for several minutes post-stimulation (see Section S5, Supporting Information).

Each tested device consisted of four arrays, 32 channels each, with a USNW pitch of 5, 10, 30, and 70 μm (Groups A, B, C, and D, respectively, Figure S4a–d, Supporting Information).

2.2. In Vitro Culture Recordings

2.2.1. Recordings from Rat Cortical Neurons

Multiple in vitro cultures from dissociated rat cortical neurons were recorded starting at 7 DIV. Recordings performed from 11 to 19 DIV exhibited diverse characteristics of biphasic and positive monophasic APs (Figure 3a–h). The raw signals show peak-to-peak amplitudes ranging from approximately 500 μV to 1 mV and upwards toward 10–12 mV. The maximum recorded potentials were truncated by the Intan amplifier recording limit of ±6.4 mV. Using USNW arrays with a different type of recording system, we have previously recorded isolated APs with 99 mV amplitude;^[26] it is likely that the maximum amplitudes of the AP reported in this work exceed the ±6.4 mV limits of our recording system. The diverse waveform characteristics on adjacent channels at 11 DIV (Figure 3a) illustrate minimal cross-coupling in between channels in our USNW arrays. We demonstrate representative recordings from all 32 channels in group B (single array with 32 USNWs at 10 μm pitch) from 11 to 19 DIV (Figure 3a–h). At earlier than 11 DIV (Figure 3a), we only observed a limited number of USNWs with intracellular activity (15/32 channels, determined by the amplitude and waveforms being recorded by each channel over 240 s). Starting from 13 DIV and onwards toward 19 DIV, almost all channels exhibited similar intracellular waveforms (31/32, 32/32, and 31/32 channels respectively for 13, 15, and 19 DIV), indicating synchronous AP firing and intimate, intracellular USNW–neuron interfaces. Development of multilayered neural networks is observed directly by a gradual increase in spike frequency with the neurons getting mature (Figure 3d,f,h and Figure S25b–d, Supporting Information) and the evolution of cross-correlation between the channels from low to high synchrony (Figure S25e–h, Supporting Information). The synchronized neuronal activity is a common phenomenon in neuronal cultures with multielectrode arrays^[41] and is related to the stage of neuron development and the neuron–glia interactions,^[41,42] and plays a crucial role in complex brain function and neurological diseases.^[43–45] The observed spike synchronicity likely originated from our multilayered, largely neuronal cultures (Figure S12, Supporting Information) with reduced isolation between neurons by glia and without the in vivo molecular heterogeneity composed of extracellular matrices that usually result in heterogeneity in firing in the brain. Thus, 13 and 15 DIV traces show two or multiple continuous spikes. Clear variance in spike counts across 32 channels in Figure 3g at

leading to smoothening of the surface of the USNWs in the array and the reduction of their diameter to sub-10 nm. g) SEM image of a sub-10 nm Si USNW tip prior to Pt coating. h) SEM image of a single Si USNW showing the tapered structure and exposed Pt tip, and i) overall view of Si USNW array. j–o) Colorized SEM images after rat cortical neuron cell fixation showing j) morphology of the cultured rat cortical neurons exhibiting high-density and neurite growth evidencing healthy cell culture and successful network formation, k) cross-section of the cultured neurons exhibiting a multilayer structure, l) “satellite”-like interconnected multilayer structures on the substrate surface, m) sequential FIB sectioning revealing first the tip of the USNW inside the soma and n) the whole USNW/neuron cross-section, o) wide-view SEM image showing the relative position of multiple USNW electrode with respect to the neuron’s somas.

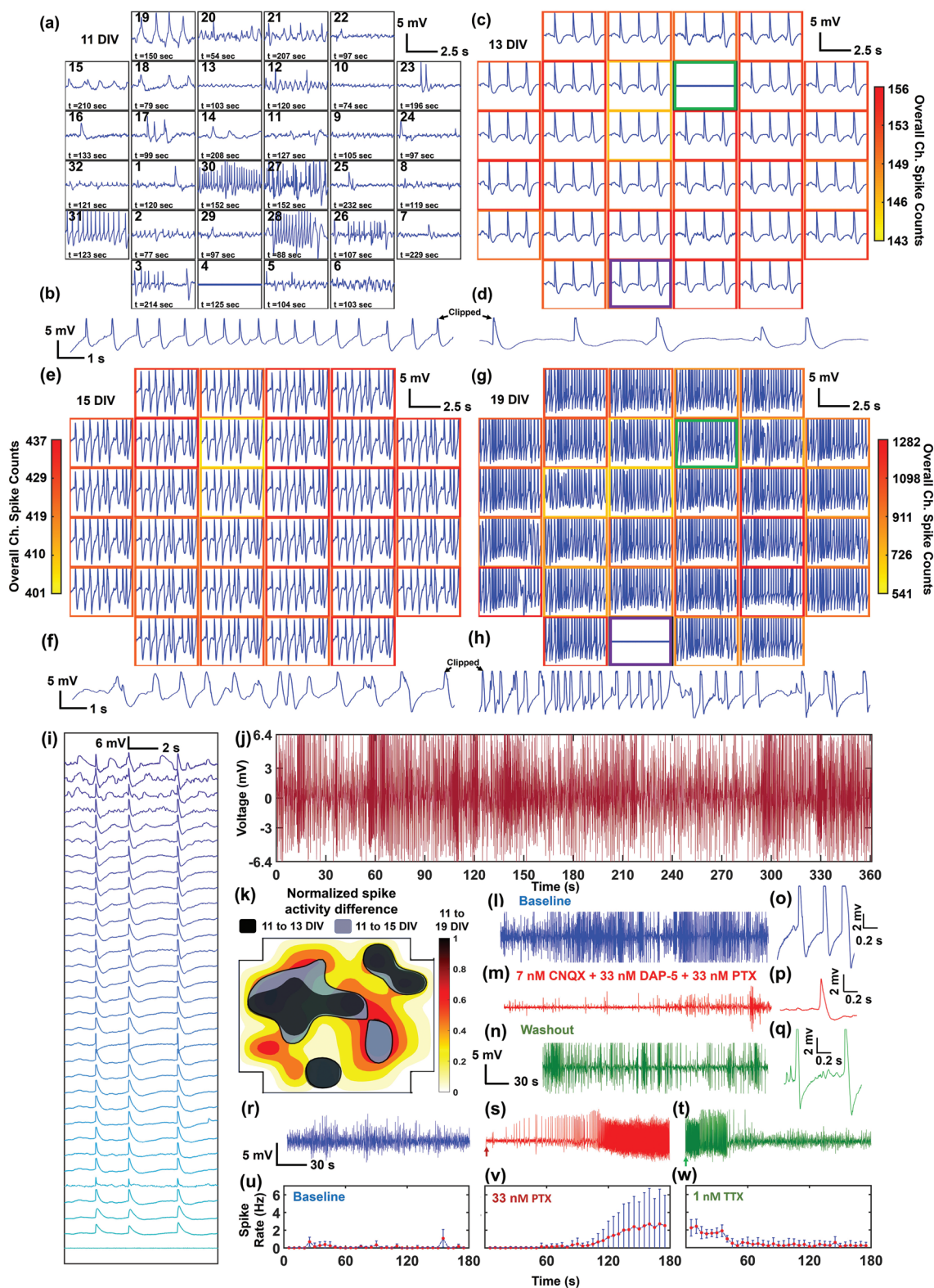


Figure 3. Example electrophysiological recording from one array (pitch = 10 μm) and pharmacological interpellation. a,c,e,g) Overall 5 s electrophysiological recording segments of multiple USNWs from group B (10 μm electrode pitch) at 11, 13, 15, and 19 DIV respectively. b,d,f,h) Close-up image of a 7 s recording segment of selected channel 31 from group B exhibiting intracellular AP waveforms at 11, 13, 15, and 19 DIV respectively. a) Overall 5 s recording segments at 11 DIV (different time segments are plotted for each channel to illustrate the overall electrophysiological activities at 11 DIV). b) Close-up image of 7 s recording segment, 11 DIV. c) Overall 5 s recording segments at 13 DIV. d) Close-up image of 7 s recording segment, 13 DIV. The

19 DIV and the evident variations in graded subthreshold potentials before AP spikes in Figure 3i confirm nonshorted, strong intracellular USNW–neuron interfaces across the recorded channels. This is further corroborated with the evidence presented in this work that shorted nanowires must exhibit small AP amplitudes (Figure 5). By taking the difference in the spike counts (across the recording duration of 240 s) measured from each channel at 13, 15, and 19 DIV to the spike counts of the same channel at 11 DIV, a contour map across the USNW placement is obtained (Figure 3k and Figure S19, Supporting Information); for longer culture duration, we observed expansion of contour regions from 13 to 19 DIV, signifying an increase in regions of spike activities from few local areas towards the majority of the USNW array. Between different recording days, channels observed shift in USNW–neuron interface conditions (visibly seen for channels 12 and 4 respectively in Figure 3c,g), corresponding to either neuron movement during culture or medium changes between days, which thereby may have exposed the particular USNWs to the culture medium. A representative channel of 7 s recording segment exhibiting significant intracellular-like APs is shown in Figure 3b,d,f,h across 11–19 DIV.

In addition, the electrophysiological activity can be strongly modulated by pharmacological intervention. On 7 DIV, the addition of the gamma aminobutyric acid (GABA) subtype A (GABA_A) receptor antagonist picrotoxin (PTX; 33×10^{-9} M) gradually increased the frequency and the amplitude of APs, consistent with the loss of GABAergic inhibition (Figure 3s). In contrast, we found that the addition of the sodium channel blocker tetrodotoxin (TTX; 1×10^{-9}) suppressed firing (Figure 3t). To quantitatively evaluate the effect of pharmacological intervention, we implemented an autothresholding algorithm^[46–48] on the high-pass filtered recorded waveforms from 32 channels, with a criterion of positive/negative threshold of amplitudes above standard deviation values of the baseline oscillation by 4–6.5 σ . As expected, the addition of PTX increased the spike frequency against the baseline recording (Figure 3v) and the application of TTX decreased the spike firing rates (Figure 3w). The change of electrophysiological activity after the drug applications lagged for both PTX and TTX, most likely due to the inherent delay arising from diffusion time of the applied drug molecules through overlaying neuronal layers (Figure 2k) to reach the bottom-most layer of recorded neurons. Additionally, on 8 DIV, another pharmacology modulation study was performed to validate that the pre-spike activities observed at Figure S18c–e (Supporting Information) were excitatory postsynaptic potentials (EPSPs). Starting from baseline

recording with clear AP activities (Figure 3l,o), solutions of cyanquinoxaline (CNQX; 7×10^{-9} M), D(-)-2-amino-5-phosphonopentanoic acid (D-AP5; 33×10^{-9} M), and picrotoxin (PTX; 33×10^{-9} M) were added to respectively block α -amino-3-hydroxy-5-methyl-4-isoxazolepropionic acid, N-methyl-D-aspartate, and GABA_A receptors. Following their applications, there were clear decrease in AP and prepotential activities, as shown in Figure 3m,p and with a noticeable reduction in spike frequency as shown in Figure S21g–i (Supporting Information). After washout, the AP and pre-spike activities recover (Figure 3n,q), signifying that the pre-spike activities observed previously were most likely EPSPs.

Overall, we observed more than 46000 intracellular AP spikes from the rat cortical neurons across 11–19 DIV on the 32 channels of group B. The longest recording segments with continuous, intracellular activities were approximately 6 min (Figure 3j and Figure S25, Supporting Information). Our measured APs retain their amplitudes and shapes over the duration of the recording (Figure 3j and Figure S18, Supporting Information). The histogram of the interspike interval (Figure S18c, Supporting Information) reveals variability in spike bursting and an exponentially decaying tail, corresponding to AP refractory periods and spike triggering from random processes, alternating between resting and spiking phases. The mean and mode of the interspike intervals (Figure S18g, Supporting Information) range from 500 to 700 ms. For a long recording segment at 11 DIV (Figure S18a, Supporting Information), in the first 2 s time snippet (Figure S18b, Supporting Information), we observed multiple lower-amplitude spikes within the dampened and broadened temporal response of the USNW array. Such spikes likely correspond to the superposition of high-frequency AP spikes that are faster than the temporal response of the USNW array and in some recordings appeared at a small-time offset from the peak of the AP (e.g., Figure 3h). For this channel, the spike rate was then modulated and was terminated at ≈ 210 s. Smaller amplitude potentials that were recorded prior and within the spike trains appear after the 210 s (Figure S18f, Supporting Information).

Given that our recording setup is limited to measuring amplitudes below 6.4 mV, we assessed the temporal spread of the waveforms, because it is well established in USNW recordings that longer AP durations are associated with larger AP amplitudes. We compared AP spikes above and below 5 mV, considering that the best amplifier linearity for the Intan amplifier is found was between -5 and 5 mV. Below 5 mV, the temporal spread has a distribution centered around 50 ms whereas those above 5 mV exhibited a temporal spread centered around 75 ms

potential shift in USNW–neuron interface is illustrated with green and purple borders (channels 12 and 4, respectively) between 13 and 19 DIV. e) Overall 5 s recording segments at 15 DIV. f) Close-up image of 7 s recording segment, 15 DIV. g) Overall 5 s recording segments at 19 DIV, exhibiting wide variance in spike counts across channels. h) Close-up image of 7 s recording segment, 19 DIV. i) Waterfall plot of APs and varying subthreshold potentials arranged in a descending order across 32 channels from group B at 19 DIV. j) Continuous, 6 min recording segment from channel 31 USNW from group B (10 μ m electrode pitch) at 19 DIV, showing consistent high amplitude without attenuation. k) Contour map of normalized spike activity differences of 32 channels from 13, 15, and 19 DIV with spike activities from corresponding channels at 11 DIV, group B. The black, blue, and red contours represent regions exhibiting spike activity increases from 11 to 13 DIV, 11 to 15 DIV, and 11 to 19 DIV respectively. Contour colormap from 19 DIV is depicted (normalized to the maximum spike activity difference across 32 channels). l–n) Sequential recording segment of sequential pharmacological drug test performed at 8 DIV with 7×10^{-9} M CNQX, 33×10^{-9} M DAP-5, 33×10^{-9} M PTX, and 1×10^{-9} M TTX. o–q) Representative spike plots from 8 DIV from baseline recording, after CNQX, DAP-5, and PTX application, and final washout. r–t) Sequential recording segment of sequential pharmacological drug test performed at 7 DIV with 33×10^{-9} M PTX and 1×10^{-9} M TTX. The arrow pointing at the initial section mark the exact moment the drug was applied to the cultured neurons. PTX application results in heightened spike frequencies and TTX application following PTX application and recording results in reduction in spiking activities. u–w) Plots of spike rate over time for baseline, PTX, and TTX recording segments. Spike rate change according to pharmacological drug applications.

(Figure S20a, Supporting Information), further suggesting the high sensitivity of our intracellular USNWs. There is a noticeable distribution difference in the spike width, providing evidence the signals were indeed clipped and with a recording system with greater limits, the amplitude would have been larger than what was recorded.

2.2.2. Recordings from iPSC-Derived Cardiovascular Progenitor Cells

We further investigated the capabilities of our USNW array platform in recording intracellular and network-level activity in vitro in iPSC-derived cardiovascular progenitor cells (iPSC-CVPCs)^[49] with the culture procedures detailed in Section S3.2 (Supporting Information). Figure 4a shows voltage traces for 52 channels of two separate arrays (out of 64 total channels, 32 channels per array) recorded from the iPSC-CVPCs at day 34 of differentiation (5 DIV on USNW platform). The zoom-in plot of single spikes across the array (Figure 4b) shows a clear peak time delay revealing tissue-wide propagation of APs, afforded by the high temporal resolution of the recording (0.033 ms for sampling rates at 30 kS s^{-1}). Similar to the electrophysiological recordings from neurons, significant intracellular amplitudes from the iPSC-CVPCs were also recorded for the overall

duration of the experiment. The maximum voltage amplitudes of the APs are clipped at 6.4 mV in our Intan setup (Figure S22, Supporting Information); however, with the TDT system with its PZ5 Neurodigitizer with $\pm 500 \text{ mV}$ amplifier input range, we were able to record AP with a maximum peak-to-peak voltage of 60 mV (Figure 4e). The maximum voltage amplitudes of the representative channel at Figure 4c shows consistent firing with no amplitude decay during a 372 s recording time (beating interval of 2.05 s; Figure 4c,d). The iPSC-CVPCs' recorded APs exhibit atrial-like intracellular attributes with minimal plateau phase, shorter durations, and higher spontaneous beating rates compared to ventricular-like APs.^[50] We measured the time difference between the AP duration at 30% to 40% repolarization (APD30-40) and the time difference between APD70 to APD80 (APD70-80), and then the calculated ratio of APD30-40/APD70-80 is close to unity (Figure 4d), evidencing that the recorded shape is that of atrial-like quality. Furthermore, our iPSC-CVPCs cell line show atrial-like cell phenotype verified by immunofluorescence staining images from our past works.^[49,51] At the early stage of the iPSC differentiation, not all the ion channels are expressed; thus, the CMs cannot show signals as conveyed from mature CMs, such as ventricular-like signals with longer duration; rather, CMs at the early stage of the iPSC differentiation have demonstrated to have shorter APD.^[52] In

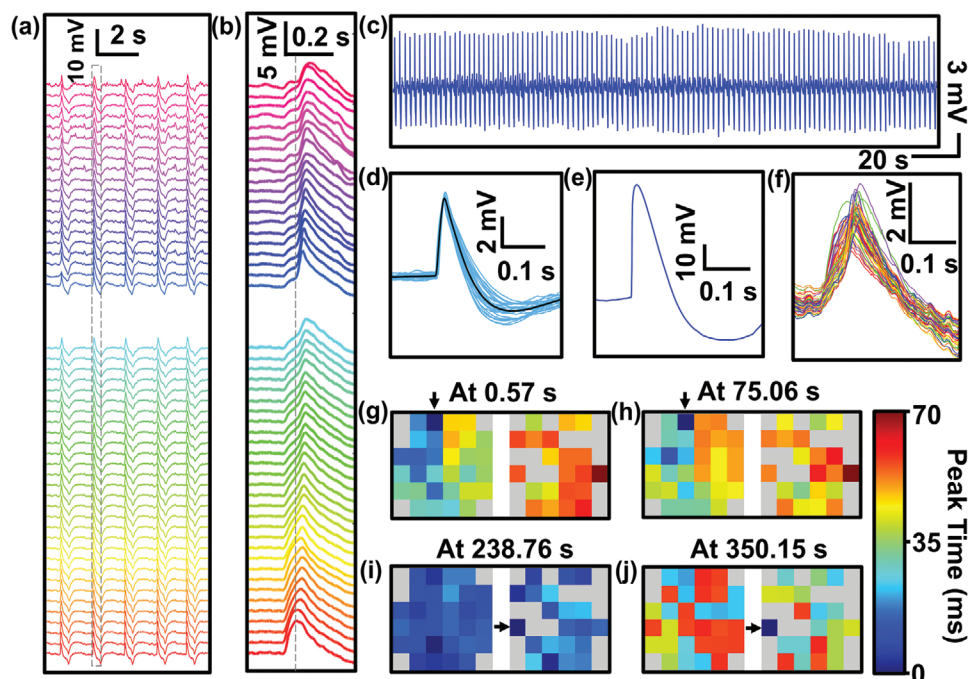


Figure 4. Network-level intracellular recording of in vitro iPSC-derived cardiovascular progenitor cells (iPSC-CVPCs) and active spatiotemporal modulation of APs. a) 52-Channel voltage traces of two arrays recorded from the iPSC-CVPCs at day 34 of differentiation (5 DIV). b) Zoom-in view of the second column of traces in a) shows a single-spiked AP recording. c) Intracellular recordings of cardiac activity from a representative channel (No. 48) show consistent spiked APs with no amplitude decay during the 372 s recording time. d) Zoom-in view of 47 randomly selected raw waveforms of a representative spike-sorting APs and spike averaged waveform, as shown in black. e) 60 mV AP measured via TDT system. f) Selected time segment of 52-channel voltage traces. g–j) Mapping of AP propagation patterns across the two arrays at different time points before (at 0.57 s in g) and at 75.06 s in h) and after (at 238.76 s in i) and at 350.15 s in j) electrical stimulation. Two intracellular recordings before electrical stimulation (at 0.57 s and at 75.06 s) show AP propagation from left to right, whereas intracellular recordings after electrical stimulation show an evolution from homogeneous propagation at 238.76 s to reversed direction that originates from right to left, where the AP propagation direction starts from the stimulating electrode. The original pacemaker foci location is labeled with arrows. The biphasic-pulse stimulation peak width, amplitude, and frequency were 0.5 ms, 10 nA, and 1 Hz, respectively.

recent research by Zhang et al.^[53] regarding iPSC-CMs differentiation with nearly identical cell type, cell age (D35), and protocol, atrial-like CM signals were recorded via patch clamp, with similar atrial-like AP shape and duration as our recorded iPSC-CVPC AP. Importantly, cells even at D60 derived in the same protocol have shown similar, atrial-like AP properties.^[53]

Our USNW platform enabled us to natively record significant intracellular potentials, demonstrating network-level intracellular recording from the tightly connected in vitro cultured iPSC-CVPCs 2D tissues (Figure S17, Supporting Information) covering two arrays of USNWs. We viewed the difference of the activation time across channels at the same time point (Figure 4f), and we mapped the AP propagation patterns across the two arrays at different time points before (at 0.57 s and at 75.06 s) and after (at 238.76 s and at 350.15 s) electrical stimulation (Figure 4g–j, and Figures S23 and S24, Supporting Information). Two intracellular recordings before electrical stimulation (at 0.57 s and at 75.06 s) show AP propagation from left to right. We used active electrical stimulation and mapping capabilities to illustrate spatial modulation of the AP propagation direction within cardiac tissues. Specifically, a USNW-cardiac tissue sample with the original pacemaker foci located at channel No. 32 (Figure 4g) was sequentially paced by stimulator electrodes located at channel No. 52 (see Figure S24c, Supporting Information). After electrical stimulation, the activity was synchronized across all channels (Figure 4i, 238.76 s) and then reversed the propagation direction from right to left (Figure 4j, at 350.15 s). The new AP propagation direction starts from the simulated electrode of channel No. 52 (see Figure S24c, Supporting Information). The biphasic-pulse stimulation peak width, amplitude, and frequency were 0.5 ms, 10 nA, and 1 Hz, respectively, applied for 10 s. The results presented here show high-spatiotemporal-resolution electrophysiological mapping and simultaneous interrogation in cardiac tissues for control of cardiac activity, and offer the potential to affect several areas of cardiac research including in vitro models for drug screening, and patient-specific models related to cardiac differentiation from progenitor cells or stem cells into damaged tissues with integrated self-mapping and self-modulation functionality.

2.3. Performance from Individual Addressability of USNWs

2.3.1. Amplitude Comparison between Numbers of USNWs per Channel

Finally, we explored the benefit of conducting recordings with individually electrically addressable USNWs. The same fabrication process was implemented for USNW electrodes with 16 and 625 USNWs shorted on a single pad/channel (Figure 5a,c,e). Rat cortical neurons were simultaneously cultured on the three types of samples and they were all recorded from 11 to 19 DIV. Sample recording traces for 10 s are shown for single USNW (Figure 5b), 16 USNWs (Figure 5d), and 625 USNWs (Figure 5f), where we observed the highest recorded APs with graded subthreshold potentials from the sample with an individual USNW per channel. The amplitude of the recorded potentials decreased with the increase of the number of USNWs per channel. To quantitatively assess the amplitudes

of the recorded APs with respect to the number of USNWs per channel, we plotted the histogram of the peak-to-peak amplitudes in a semi-log scale (Figure 5g). We selected channels exhibiting high amplitude signals (15 to 32 out of 32 channels for single USNW, 27 out of 32 channels for 16 USNWs, 30 out of 64 channels for 625 USNWs from 11 to 19 DIV), and compared amplitude distribution with a similar number of detected spikes (2133 spikes, randomly truncated without repetitions from a total of around 6000 detected spikes, from one channel for single USNW, 2133 spikes for 16 USNWs, and 1773 spikes for 625 USNWs). As with pharmacological drug-modulated data analysis, spikes were sorted through an autothreshold algorithm with bipolar thresholds (Section S6, Supporting Information). The resulting amplitude distributions for different number of USNWs per site were disparate from one another: as the number of USNWs per site decreased, the distribution of peak-to-peak amplitude increased (Figure 5g). The amplitude distributions were centered around approximately 4 mV and 9 mV, 500 μ V and 2 mV, and 60 μ V and 300 μ V for 1, 16, and 625 NWs per channel, respectively. The different amplitude distributions indicate variability in the capability of each type of USNWs for recording intracellular potentials. However, the histogram plots together with the exhibited potential waveforms clearly demonstrate that individual USNWs per channel yield the highest amplitude APs and can record subthreshold potentials. Neither of these attributes can be clearly discerned from the recordings made with 16 and 625 USNWs per channel.

2.3.2. Small Signal Circuit Modeling

The circuit models presented in Figure 5h,i demonstrate a critical design flaw with placing multiple USNWs on a single recording channel, wherein the intracellular potential can be electrically shorted to the grounded extracellular potential. This model builds off the simulations done by Hai et al.^[54] by investigating the effects of having a portion of the USNWs penetrate a cell body, while the remaining USNWs remain extracellular. The details of this model are discussed in Section S7 (Supporting Information). Using measurements of transmembrane current during an AP to ground our models, we simulated the relevant signal paths for several situations. We first modeled the ideal case where a single USNW penetrates the cell membrane and forms a tight seal. We then modeled the effects of adding up to five additional extracellular USNWs on the same recording channel. The resulting potential waveforms shown in Figure 5i demonstrated a maximum signal amplitude for the single USNW case and a decrease in amplitude as we increased the number of extracellular USNWs. Furthermore, when we plotted the ratio of the peak intracellular potential over the peak potential seen by the amplifier (a proxy for signal gain), denoted as the coupling coefficient,^[54] we saw that this coefficient decayed exponentially with increasing number of extracellular USNWs (Figure 5k). To develop intuition on the frequency-dependent signal distortion, we computed the ratio of pulse widths of the simulated signal at the input to the amplifier over that of the potential inside of the cell, which we denoted as a temporal spreading coefficient (Figure 5k). These modeling results agree well with the experimental results (Figure 5a–g).

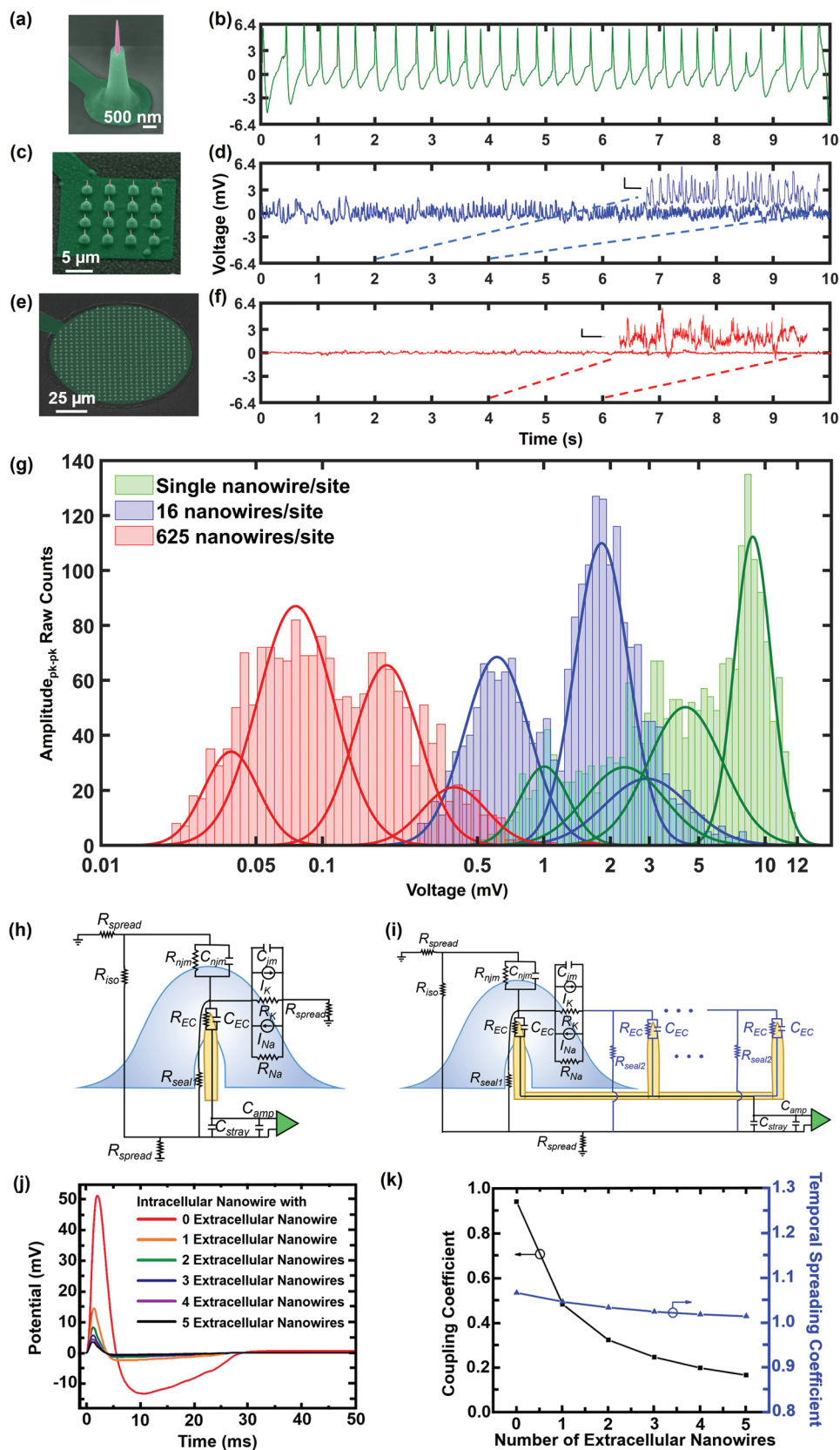


Figure 5. Sample recording traces and amplitude contrasts between individually addressable USNW and multiple USNWs per recording sites and small-signal circuit model simulation results. a–f) SEM images of individually addressable, single USNW, 16 USNWs, and 625 USNWs and sample

3. Limitations

There are three main experimental limitations in this study: The first being that our experimental setup requires recording outside the cell culture incubator, where the duration of the recording is limited to several minutes before returning the devices to the incubator in order to maintain constant temperature, CO₂ concentration, and pH levels and to avoid contamination,^[55,56] thereby excluding our ability to assess the longitudinal intracellular recording capacity. This could be tested using cell culture methods compatible with an ex-incubator environment, e.g., HEPES-buffered media and a heated recording platform. Further, sample movements inside and out of the incubator could also alter the USNW–neuron interface to positively or negatively affect the recordings (provide an intimate, intracellular interface or expose USNW to the culture medium without neuron interface respectively). This limitation can be addressed by performing recordings inside the incubator, which has been demonstrated by Abbot et al.^[10] The second limitation is that our recording amplifiers are designed for extracellular multi-electrode recordings, which do not perform parasitic capacitance cancellation, and as a result distorts the temporal fidelity of the recordings, broadens and attenuates the recorded waveforms. This could be addressed using amplifiers with a wide dynamic range for intracellular recordings from thousands of channels, which are available in research labs,^[57] where specialized circuits can be custom-designed to restore the temporal resolution of the USNWs for known USNW and parasitic impedances. Lastly, our fabrication method involved multiple dry oxidation cycles to sharpen the USNW tips at 1100 °C, which is not CMOS compatible. We envision acquisition integrated circuits to be integrated on the periphery of our USNW arrays rather than below them to maintain the capabilities and the advantages that this platform brings over the state of the art.

4. Conclusion

The present study unequivocally demonstrates a high yield fabrication process for long (>6 μm) vertical USNW arrays with sub-10 nm tips that are individually electrically addressable for electrophysiological recordings of intracellular potentials. This work demonstrates that vertical USNW arrays and individual electrical addressability can record subthreshold and APs with significant amplitudes by the natural internalization. We mapped the neuronal/cardiac intracellular activity at the single-cell resolution, observed clear synaptic network activity between neurons and cardiac activity propagation in the extended networks, manipulated the neuronal activities by

pharmacological test, and manipulated the cardiac signal propagation direction by electrical stimulation. Using both experiments and simulations, we validated that multiple USNWs per single channel reduce the amplitude and sensitivity of the recordings compared to a single USNW per channel recording. We believe that these results underscore a significant advancement in our understanding and control over the USNW–neural interface. Novel integration of the USNW with depth probes or 2D soft substrate may be applied in vivo for the potential intracellular recordings from intact brains. With the demonstrated sensitivity, this platform paves the way for novel scientific and technological undertakings that aim to establish large-scale bidirectional biotic–abiotic interfaces with intracellular access for drug screening, disease modeling, and beyond.

5. Experimental Section

USNW Electrode Design, Fabrication, Packaging, and Characterization: The Si USNW platform consists of a total of 128 channels divided into 4 subgroups with different USNW pitch of 5, 10, 30, 70 μm (Figure S4, Supporting Information) to provide a judicious range of USNW density to maximize the probability of membrane permeability by changing the electrode–neuron interface tension. Generally, a narrower pitch requires taller nanoelectrodes for effective membrane penetration, which is accounted for with our USNW's height, standing between 6 to 7 μm.^[58]

The array fabrication begins with e-beam lithography (EBL) patterning of center dots with 800 nm diameter and peripheral dots with 300 nm diameter in the resist on the prime-grade p-type doped Si substrate (Figure 2a and Figures S1 and S2, Supporting Information). 200 nm of Ni was then evaporated and lifted off, forming dot-like arrays that form the etching masks for Si. A SF₆/C₄F₈ based inductively coupled plasma (ICP)/reactive ion etching (RIE) process was then utilized to selectively etch the uncovered Si substrate by 6–7 μm to form vertically standing Si nanowires (Figures S1 and S2, Supporting Information). These nanowires initially had flat tips following the planar Ni discs. The resulting nanowires were then processed through multiple thermal oxidations and buffered oxide etch (BOE) cycles to provide smooth surface, achieve desired tapering for robust support, and thin USNW tips as shown in Figures S1 and S2 (Supporting Information). Following the USNW formation, the whole device undergoes a long, unmasked, thermal oxidation to fully oxidize the vertically standing USNWs and the surface of the substrate to electrically isolate all USNWs. Subsequently, patterns of USNW electrode and center interconnects were aligned and defined by EBL, and 10 nm/100 nm of Cr/Pt are deposited by conformal electron-beam evaporation through sample rotation to provide independent electrical addressability for each USNW (Figure S3, Supporting Information). To avoid electrochemical coupling and corrosion in the culture medium, the metal interconnects were passivated by using PECVD SiO₂. Control experiments demonstrated that a 500 nm thick SiO₂ passivation layer is needed for stable passivation against delamination in a wet environment (Figure S5, Supporting Information). Additionally, a 500 nm thick parylene C layer was employed for both passivation and improvement of adhesion

10 s recording trace from recordings performed at 11 DIV. Single USNW—channel 31 from group B (10 μm electrode pitch), 16 USNWs—channel 31 from group B (10 μm electrode pitch), 625 USNWs—channel 21 from group C (30 μm electrode pitch). Vertical scale bars for zoomed-in recording segments for 16 USNWs and 625 USNWs are: 500 μV and 200 μV respectively. The time scale bar for both segments is 250 ms. g) Histogram of peak-to-peak signal amplitude between single USNW and multi-USNWs per site. There are clear, distinguishable differences in the distribution of amplitudes. Two distributions most likely correspond to the intracellular and extracellular recording interface setup the USNW formed with the neurons. h) Circuit model of single USNW penetrating the cultured neuron. i) Circuit model of multi-USNW setup with only one USNW penetrating the cultured neuron. j) Simulated intracellular signal amplitude based on the number of extracellular USNWs connected to the intracellular USNW. k) Simulated plot of coupling coefficient and temporal spreading coefficient versus the number of extracellular USNWs. Signal attenuation decays exponentially with increasing the number of extracellular USNWs.

of cells and substrate. Both the parylene C and the SiO₂ layer were selectively etched from the USNW tips by recessing a resist layer and employing an O₂ plasma etch for parylene C and BOE etch for SiO₂, exposing the Pt coated USNW tips while the remainder of the USNW remains unaltered (Figures S6 and S7, Supporting Information). Alongside SiO₂, parylene C exhibits excellent mammalian cell adhesion properties after proper surface preparation via O₂ plasma treatment.^[40] For in vitro cell culture, the final device was bonded with a culture chamber via polydimethylsiloxane (PDMS) application to delineate the region of cell culture interest with the rest of the device. Finally, the USNW electrodes were electrically connected with flexible flat cable (FFC) via anisotropic conductive film (ACF) bonding (Figure S8, Supporting Information). The resulting USNW structure is composed of an exposed metal tip and a passivated bottom layer for good electrical isolation. The ideal USNW tips are sharpened to sub-10 nm range before conformal metal coating with proper masking and optimized etching process (Figure 2i, Figure S1f, Supporting Information). Overall, USNWs formed consistently throughout the array with uniform electrochemical impedance. A representative characterization result of the 128 channel devices showed 100% yield and average impedance of 14.95 MΩ at 1 kHz in Figure S9 (Supporting Information).

Rat Cortical Neuron Culture on USNW Array Electrodes: The integration of USNW array electrodes with cells followed immediately from fabrication and packaging of the devices, which involved the following steps (steps 1 to 4 were also applied before iPSC-CVPCs cultures):

- (1) The USNW array device was sterilized by 1) DI water rinse for three times, and 2) 70% ethanol for at least 30 min.
- (2) The device was washed with phosphate buffered saline (PBS) for three times followed by placing 20 μL drop of (0.1% w/v) polyethylenimine (PEI, Sigma-Aldrich) solution on the USNW array and incubating them at 37 °C incubator for 1 h.
- (3) The PEI was aspirated and washed with 500 μL double distilled water (ddH₂O) for four times. The device was dried in the incubator for 5 h per overnight.
- (4) A spot of 20 μL laminin (20 μg mL⁻¹, Sigma-Aldrich) was added to the USNW array and incubated at 37 °C for 1 h.
- (5) Neuronal cell culture medium (Neurobasal (Thermo Fisher Scientific) +2% B27 (Thermo Fisher Scientific) +1% P/S (Corning) + 10% FBS) was prepared for plating rat cortical neurons on the USNW arrays.
- (6) The cryopreserved rat neurons cryovial (from Thermo Fisher Scientific) was removed from the liquid nitrogen storage container, warmed in a 37 °C water bath for exactly 2.5 min, sprayed the outside with 70% ethanol, wiped dry, and placed in a tissue culture hood.
- (7) The contents of the cryovial were carefully transferred to a 15 mL centrifuge tube using a 1 mL pipettor. The inside of the cryovial was carefully washed with 1 mL of room temperature neuronal cell culture medium (≈1 drop s⁻¹). 3 mL of room temperature neuronal cell culture medium was slowly added to the tube (≈1–2 drops s⁻¹). The contents were carefully mixed by inverting the tube two to three times. The total number of cells in suspension was determined via hemocytometer count.
- (8) The cells were concentrated by centrifuging at 1100 rpm for 3 min. Laminin was aspirated and 20 μL cell suspension was plated directly on the USNW arrays with the cell density at 200k cells per array. The USNW devices with seeded neurons were incubated in a cell culture incubator at 37 °C, 5% CO₂ for 40–50 min. Next, 500 μL of warm neurobasal medium was carefully added to the chamber from the side of the device. To avoid adding the medium too fast to cause the detachment of the adhered neurons on the USNWs, the USNW devices with seeded neurons were put back to the cell culture incubator at 37 °C, 5% CO₂ for another 35–40 min. Then, another 500 μL of warm neurobasal medium was carefully added to chamber from the side of the device to reach a volume of 1.5 mL per device. Finally, the USNW devices with seeded neurons were put back to the cell culture incubator at 37 °C, 5% CO₂.

- (9) On the next day, the medium was changed to Brainphys Complete (Brainphys basal medium (Stemcell technologies) +1% N2 supplement (ThermoFisher) +2% B27 supplement (ThermoFisher) +1% Pen/Strep (Gibco/Life Technologies)) with the addition of the following supplements: Brain-derived neurotrophic factor (BDNF, 20 ng mL⁻¹; Peprotech), Glia-derived neurotrophic factors (GDNF, 20 ng mL⁻¹; Peprotech), ascorbic acid (AA, 200 × 10⁻⁹ M; Sigma-Aldrich), dibutyryl cyclic AMP (cAMP, 1 × 10⁻³ M Sigma-Aldrich) and laminin (1 μg mL⁻¹; Invitrogen). Then, half the medium was replaced with fresh medium every other day with Brainphys Complete and supplements until 7 DIV, then switched back to Brainphys Complete with no added supplements.

FIB-SEM Characterization of USNW–Neuron Interface: To precisely investigate the biological interface formed between the USNWs and the cultured neurons after the completion of electrophysiological recording sessions, a sequential FIB cut was performed to reveal the cross-section of USNW regions after appropriate Pt plating for protection from ion-milling damages. The successive FIB cuts showed both proper engulfment and clear intracellular penetration of the USNW into the cultured rat neurons' soma, which aligned well to the positive-phase potentials measured in the electrophysiological recordings, shown in the followed analysis. The intracellular nanoelectrode–neuron interface observed here was based on native penetration deriving from the ultrasharp USNW tips, without any additional surface chemical treatments such as peptide-modification^[59] and widespread electroporation for increased cell membrane permeability. The SiO₂ USNWs were rigid and free-standing for stable interaction with the neurons without any USNW breakage.

Neuronal Recording and Pharmacological Drug Application: Three minutes of baseline activity was recorded, followed by 33 × 10⁻⁹ M application of the GABA_A-R blocker picrotoxin (PTX, Tocris) to the device chamber. The activity was then recorded for 3 to 5 min to observe the effect of blocking inhibition on the electrical activity of the neuronal network. Finally, 1 × 10⁻⁹ M tetrodotoxin (TTX, Abcam) was added to the solution to block voltage-gated sodium channels (Na_v) and prevent generation of APs.

Supporting Information

Supporting Information is available from the Wiley Online Library or from the author.

Acknowledgements

R.L., J.L., and Y.T. contributed equally to this work. This work was performed with the gracious support of National Science Foundation Award No. 1728497 under the stewardship of Dr. Khershed Cooper and of the National Institutes of Health Award No. NBIB DP2-EB029757 under the stewardship of Dr. Michael Wolfson. S.A.D., J.S.M., and R.L. also acknowledge the gracious support of the UC-National Laboratory in Residence Graduate Fellowships (UC-NLGF), Award No. 477131. This work was performed, in part, at the Center for Integrated Nanotechnologies, an Office of Science User Facility operated for the U.S. Department of Energy (DOE) Office of Science. Los Alamos National Laboratory, an affirmative action equal opportunity employer, is managed by Triad National Security, LLC for the U.S. Department of Energy's NNSA, under contract 89233218CNA000001 and Sandia National Laboratories (Contract No. DE-AC04-94AL85000) through a CINT user proposal. This work was performed in part at the San Diego Nanotechnology Infrastructure (SDNI) of UCSD, a member of the National Nanotechnology Coordinated Infrastructure, which is supported by the National Science Foundation (Grant ECCS-1542148). The authors thank technical support from the Integration Laboratory at CINT and from the nano3 clean room facilities at UC San Diego's Qualcomm Institute. R.L. and S.A.D. acknowledge inspiring technical

discussions with Dr. Renjie Chen, and Dr. Atsunori Tanaka, as well as discussions and technical support from Dr. Katherine L. Jungjohann, Anthony R. James, Douglas V. Pete, and Denise B. Webb of Sandia National Laboratories. S.A.D. conceived and led all aspects of the project. R.L. developed the fabrication process with S.A.D. R.L. fabricated the platform with input and training from J.N., J.Y., M.L.P. and J.S.M.; Y.G.R., Y.T. and L.A.H. participated in the fabrication; R.L. performed the FIB sectioning and SEM imaging. R.L. and R.V. performed electrochemical characterization; R.L. and S.H.L. performed electrophysiological recordings; D.P. and G.R. cultured the primary rodent neurons under supervision of A.G.B.; A.D.C. cultured iPSC-derived cardiovascular progenitor cells under the supervision of K.A.F.; A.M.B., Y.T. and S.A.D. carried out the electrochemical interface modeling. J.L., Y.T., R.L., K.J.T., and S.A.D. analyzed the data and wrote the manuscript. All authors discussed the results and contributed to the manuscript writing.

Conflict of Interest

The authors declare no conflict of interest.

Data Availability Statement

The data that support the findings of this study are available from the corresponding author upon reasonable request.

Keywords

cardiomyocytes, culture, intracellular, nanowires, neurons, tissues

Received: August 21, 2021

Revised: September 26, 2021

Published online:

- [1] M. Steriade, I. Timofeev, F. Grenier, *J. Neurophysiol.* **2001**, *85*, 1969.
- [2] E. Neher, B. Sakmann, J. H. Steinbach, *Pflügers Arch.* **1978**, *375*, 219.
- [3] M. Martina, I. Vida, P. Jonas, *Science* **2000**, *287*, 295.
- [4] D. Henze, G. Buzsaki, *Neuroscience* **2001**, *105*, 121.
- [5] A. Hai, J. Shappir, M. E. Spira, *Nat. Methods* **2010**, *7*, 200.
- [6] J. T. Robinson, M. Jorgolli, A. K. Shalek, M.-H. Yoon, R. S. Gertner, H. Park, *Nat. Nanotechnol.* **2012**, *7*, 180.
- [7] M. E. Spira, N. Shmoel, S.-H. M. Huang, H. Erez, *Front. Neurosci.* **2018**, *12*, 212.
- [8] C. Xie, Z. Lin, L. Hanson, Y. Cui, B. Cui, *Nat. Nanotechnol.* **2012**, *7*, 185.
- [9] X. Duan, R. Gao, P. Xie, T. Cohen-Karni, Q. Qing, H. S. Choe, B. Tian, X. Jiang, C. M. Lieber, *Nat. Nanotechnol.* **2012**, *7*, 174.
- [10] J. Abbott, T. Ye, K. Krenak, R. S. Gertner, S. Ban, Y. Kim, L. Qin, W. Wu, H. Park, D. Ham, *Nat. Biomed. Eng.* **2020**, *4*, 232.
- [11] B. Desbiolles, E. de Coulon, A. Bertsch, S. Rohr, P. Renaud, *Nano Lett.* **2019**, *19*, 6173.
- [12] B. X. Desbiolles, E. de Coulon, N. Maïno, A. Bertsch, S. Rohr, P. Renaud, *Microsyst. Nanoeng.* **2020**, *6*, 67.
- [13] M. Dipalo, H. Amin, L. Lovato, F. Moia, V. Caprettini, G. C. Messina, F. Tantussi, L. Berdondini, F. De Angelis, *Nano Lett.* **2017**, *17*, 3932.
- [14] M. Dipalo, S. K. Rastogi, L. Matino, R. Garg, J. Bliley, G. Iachetta, G. Melle, R. Shrestha, S. Shen, F. Santoro, *Sci. Adv.* **2021**, *7*, eabd5175.
- [15] Z. C. Lin, A. F. McGuire, P. W. Burridge, E. Matsa, H.-Y. Lou, J. C. Wu, B. Cui, *Microsyst. Nanoeng.* **2017**, *3*, 1.
- [16] Q. Qing, Z. Jiang, L. Xu, R. Gao, L. Mai, C. M. Lieber, *Nat. Nanotechnol.* **2014**, *9*, 142.
- [17] Y. Zhao, S. S. You, A. Zhang, J.-H. Lee, J. Huang, C. M. Lieber, *Nat. Nanotechnol.* **2019**, *14*, 783.
- [18] W. J. Tyler, *Nat. Rev. Neurosci.* **2012**, *13*, 867.
- [19] X. Xie, A. M. Xu, M. R. Angle, N. Tayebi, P. Verma, N. A. Melosh, *Nano Lett.* **2013**, *13*, 6002.
- [20] W. Kim, J. K. Ng, M. E. Kunitake, B. R. Conklin, P. Yang, *J. Am. Chem. Soc.* **2007**, *129*, 7228.
- [21] G. Piret, M.-T. Perez, C. N. Prinz, *Biomaterials* **2013**, *34*, 875.
- [22] L. Hanson, Z. C. Lin, C. Xie, Y. Cui, B. Cui, *Nano Lett.* **2012**, *12*, 5815.
- [23] L. Gällentoft, L. M. Pettersson, N. Danielsen, J. Schouenborg, C. N. Prinz, C. E. Linsmeier, *Biomaterials* **2015**, *42*, 172.
- [24] F. Patolsky, B. P. Timko, G. Yu, Y. Fang, A. B. Greytak, G. Zheng, C. M. Lieber, *Science* **2006**, *313*, 1100.
- [25] T. Cohen-Karni, Q. Qing, Q. Li, Y. Fang, C. M. Lieber, *Nano Lett.* **2010**, *10*, 1098.
- [26] R. Liu, R. Chen, A. T. Elthakeb, S. H. Lee, S. Hinckley, M. L. Khraiche, J. Scott, D. Pre, Y. Hwang, A. Tanaka, *Nano Lett.* **2017**, *17*, 2757.
- [27] H.-Y. Lou, W. Zhao, Y. Zeng, B. Cui, *Acc. Chem. Res.* **2018**, *51*, 1046.
- [28] R. Capozza, V. Caprettini, C. A. Gonano, A. Bosca, F. Moia, F. Santoro, F. De Angelis, *ACS Appl. Mater. Interfaces* **2018**, *10*, 29107.
- [29] J. Hermiz, L. Hossain, E. M. Arneodo, M. Ganji, N. Rogers, N. Vahidi, E. Halgren, T. Q. Gentner, S. A. Dayeh, V. Gilja, *Front. Neurosci.* **2020**, *14*, 55.
- [30] M. Ganji, A. C. Paulk, J. C. Yang, N. W. Vahidi, S. H. Lee, R. Liu, L. Hossain, E. M. Arneodo, M. Thunemann, M. Shigyo, *Nano Lett.* **2019**, *19*, 6244.
- [31] L. Hossain, M. Thunemann, K. Lee, S. Dayeh, A. Devor, *Proc. SPIE* **2021**, *11629*, 1162929.
- [32] S. B. Ryu, A. C. Paulk, J. C. Yang, M. Ganji, S. A. Dayeh, S. S. Cash, S. I. Fried, S. W. Lee, *J. Neural Eng.* **2020**, *17*, 056036.
- [33] N. Rogers, J. Hermiz, M. Ganji, E. Kaestner, K. Kılıç, L. Hossain, M. Thunemann, D. R. Cleary, B. S. Carter, D. Barba, *PLoS Comput. Biol.* **2019**, *15*, e1006769.
- [34] A. C. Paulk, J. C. Yang, D. R. Cleary, D. J. Soper, M. Halgren, A. R. O'Donnell, S. H. Lee, M. Ganji, Y. G. Ro, H. Oh, *Cereb. Cortex* **2021**, *31*, 3678.
- [35] J. C. Yang, A. C. Paulk, P. Salami, S. H. Lee, M. Ganji, D. J. Soper, D. Cleary, M. Simon, D. Maus, J. W. Lee, B. V. Nahed, P. S. Jones, D. P. Cahill, G. R. Cosgrove, C. J. Chu, Z. Williams, E. Halgren, S. Dayeh, S. S. Cash, *Clin. Neurophysiol.* **2021**, *132*, 2916.
- [36] J. Hermiz, N. Rogers, E. Kaestner, M. Ganji, D. R. Cleary, B. S. Carter, D. Barba, S. A. Dayeh, E. Halgren, V. Gilja, *NeuroImage* **2018**, *176*, 454.
- [37] M. Ganji, E. Kaestner, J. Hermiz, N. Rogers, A. Tanaka, D. Cleary, S. H. Lee, J. Snider, M. Halgren, G. R. Cosgrove, *Adv. Funct. Mater.* **2018**, *28*, 1700232.
- [38] S. P. Khan, G. G. Auner, G. M. Newaz, *Nanomed.: Nanotechnol., Biol. Med.* **2005**, *1*, 125.
- [39] S. Bonde, T. Berthing, M. H. Madsen, T. K. Andersen, N. Buch-Månson, L. Guo, X. Li, F. Badique, K. Anselme, J. Nygård, *ACS Appl. Mater. Interfaces* **2013**, *5*, 10510.
- [40] T. Y. Chang, V. G. Yadav, S. De Leo, A. Mohedas, B. Rajalingam, C.-L. Chen, S. Selvarasah, M. R. Dokmeci, A. Khademhosseini, *Langmuir* **2007**, *23*, 11718.
- [41] Y.-T. Huang, Y.-L. Chang, C.-C. Chen, P.-Y. Lai, C. Chan, *PLoS One* **2017**, *12*, e0187276.
- [42] D. Lam, H. A. Enright, J. Cadena, S. K. Peters, A. P. Sales, J. J. Osburn, D. A. Soscia, K. S. Kulp, E. K. Wheeler, N. O. Fischer, *Sci. Rep.* **2019**, *9*, 4159.
- [43] M. D. Tang-Schomer, T. Jackvony, S. Santaniello, *Front Neurosci.* **2018**, *12*, 630.
- [44] M. Wachowiak, D. Wesson, N. Pírez, J. Verhagen, R. Carey, *Ann. N. Y. Acad. Sci.* **2009**, *1170*, 286.
- [45] M. Bonnefond, S. Kastner, O. Jensen, *eNeuro* **2017**, *4*, 0153-16.2017.
- [46] J. M. Tanskanen, F. E. Kapucu, I. Vornanen, J. A. Hyttinen, in *2016 24th European Signal Processing Conf. (EUSIPCO)*, IEEE, Piscataway, NJ **2016**, p. 662.

- [47] J. M. Tanskanen, F. E. Kapucu, J. A. Hyttinen, in *2015 7th Int. IEEE/EMBS Conf. on Neural Engineering (NER)*, IEEE, Piscataway, NJ **2015**, p. 1016.
- [48] J. M. Tanskanen, F. E. Kapucu, I. Vornanen, K. Lenk, J. Hyttinen,
- [49] A. D'Antonio-Chronowska, M. K. Donovan, W. W. Y. Greenwald, J. P. Nguyen, K. Fujita, S. Hashem, H. Matsui, F. Soncin, M. Parast, M. C. Ward, *Stem Cell Rep.* **2019**, *13*, 924.
- [50] M. X. Doss, J. M. Di Diego, R. J. Goodrow, Y. Wu, J. M. Cordeiro, V. V. Nesterenko, H. Barajas-Martinez, D. Hu, J. Urrutia, M. Desai, *PLoS One* **2012**, *7*, e40288.
- [51] A. D'Antonio-Chronowska, M. D'Antonio, K. A. Frazer, *Bio-Protoc.* **2020**, *10*, e3755.
- [52] J. Ma, L. Guo, S. Fiene, B. Anson, J. Thomson, T. Kamp, K. Kolaja, B. Swanson, C. January, *Am. J. Physiol.* **2011**, *301*, 599.
- [53] J. Z. Zhang, V. Termglinchan, N.-Y. Shao, I. Itzhaki, C. Liu, N. Ma, L. Tian, V. Y. Wang, A. C. Chang, H. Guo, *Cell Stem Cell* **2019**, *24*, 802.
- [54] A. Hai, A. Dormann, J. Shappir, S. Yitzchaik, C. Bartic, G. Borghs, J. Langedijk, M. E. Spira, *J. R. Soc., Interface* **2009**, *6*, 1153.
- [55] D. K. Rajan, J. Verho, J. Kreutzer, H. Välimäki, H. Ihalainen, J. Leikkala, M. Patrikoski, S. Miettinen, in *2017 IEEE Int. Symp. on Medical Measurements and Applications (MeMeA)*, IEEE, Piscataway, NJ **2017**, p. 470.
- [56] J. Michl, K. C. Park, P. Swietach, *Commun. Biol.* **2019**, *2*, 144.
- [57] J. Wang, A. Paul, D. Zhang, J. Wu, Y. Xu, Y. Zou, C. Kim, G. Cauwenberghs, in *2020 IEEE Symp. on VLSI Circuits*, IEEE, Piscataway, NJ **2020**, p. 1.
- [58] M. L. Khraiche, R. H. El Hassan, *J. Sci.: Adv. Mater. Devices* **2020**, *5*, 279.
- [59] J.-H. Lee, A. Zhang, S. S. You, C. M. Lieber, *Nano Lett.* **2016**, *16*, 1509.

Supporting Information

for *Adv. Funct. Mater.*, DOI: 10.1002/adfm.202108378

Ultra-Sharp Nanowire Arrays Natively Permeate,
Record, and Stimulate Intracellular Activity in Neuronal
and Cardiac Networks

*Ren Liu, Jihwan Lee, Youngbin Tchoe, Deborah Pre,
Andrew M. Bourhis, Agnieszka D'Antonio-Chronowska,
Gaelle Robin, Sang Heon Lee, Yun Goo Ro, Ritwik
Vatsyayan, Karen J. Tonsfeldt, Lorraine A. Hossain, M.
Lisa Phipps, Jinkyong Yoo, John Nogan, Jennifer S.
Martinez, Kelly A. Frazer, Anne G. Bang, and Shadi A.
Dayeh**

Supporting Information

Ultra-Sharp Nanowire Arrays Natively Permeate, Record, and Stimulate Intracellular Activity in Neuronal and Cardiac Networks

*Ren Liu, Jihwan Lee, Youngbin Tchoe, Deborah Pre, Andrew M. Bourhis, Agnieszka D'Antonio-Chronowska, Gaelle Robin, Sang Heon Lee, Yun Goo Ro, Ritwik Vatsyayan, Karen J. Tonsfeldt, Lorraine A. Hossain, M. Lisa Phipps, Jinkyoungh Yoo, John Nogan, Jennifer S. Martinez, Kelly A. Frazer, Anne G. Bang, Shadi A. Dayeh**

This file includes Supplementary Methods, Supplementary Figures, and Supplementary References:

1. Fabrication, optimization process and packaging of individually electrically addressable Si USNW array devices

- 1.1 RIE/ICP dry etching and thermal oxidation processes for Si USNW etching, thinning, and sharpening.
- 1.2 Fabrication for electrodes and metal interconnects.
- 1.3 Optimization of passivation.
- 1.4 Surface roughness optimization
- 1.5 Packaging of the USNW array device and FFC Bonding

2. Electrochemical characterizations of individually electrically addressable Si USNW array devices

- 2.1 1 kHz electrochemical impedance assessment across arrays
- 2.2 Electrochemical impedance spectroscopy and charge injection capacity

3. Cell Culture, pharmacological stimulation and inhibition

- 3.1 Rat cortical neuron culture on USNW array devices
- 3.2 iPSC-CVPCs culture on USNW array devices
- 3.3 Pharmacological stimulation and inhibition

4. SEM and FIB-SEM imaging on neurophysiology platform

5. Electrophysiological recordings of neuron and cardiomyocyte activity

6. Channel selection and auto-threshold spike sorting

- 6.1 Channel selection via cross-correlation matrix
- 6.2 Auto-threshold spike sorting
- 6.3 Misc. data analysis from detected spikes

7. Small signal circuit modeling of individually addressable USNW versus multi-USNWs per channel

8. References

1. Fabrication, optimization process and packaging of individually electrically addressable Si USNW array devices

1.1 RIE/ICP dry etching and thermal oxidation processes for Si USNW etching, thinning, and sharpening.

We performed mechanistic studies to obtain tapered USNWs with a larger base diameter, since the inverted cone structure provides the USNWs enough mechanical strength and stabilizes the USNWs' shape and potentially the electrical interface with neurons. The overview of the key fabrication process steps is shown in the schematic figures in Figure S1a-h, with cross-sectional overview of the fabricated USNW shown in Figure S1i. Initially, dot patterns (center dot diameter was 800 nm and peripheral dot diameter was 300 nm) and alignment markers were patterned on the Si substrate by using JEOL EBL (JBX-6300FS), and Ti/Ni (10 nm/ 200 nm) was deposited by using electron-beam evaporation (Figure S1j). After lift-off in acetone for 2 hours, samples were cleaned by IPA and N₂ blow dry. Next, USNWs and markers were etched by using Plasmatherm SLR-770 DRIE / ICP Etcher (Figure S1k). The reactive-ion etching (RIE) power was 10 W, the inductively coupled plasma (ICP) power was 700 W, the chamber pressure was 23 mTorr, the electrode temperature was 20 °C, the gas flow of SF₆, C₄F₈, Ar were 20 sccm, 40 sccm and 40 sccm, respectively (etch rate is 110 nm min⁻¹). Then, we used diluted nitric acid (HNO₃:H₂O = 1:10) to etch the Ni etching mask residue, followed by cleaning polymer residue from the Si NW etch with Piranha solution (sulfuric acid 30%:hydrogen peroxide solution = 3:1), rinsing with deionized water, drying with N₂ gas (Figure S1l). Next, the sample was placed on a quartz boat and loaded into a thermal oxidation furnace tube. The thermal oxidation temperature was 1100 °C. A layer of SiO₂ was formed at the surfaces of the NW and of the substrate after the thermal oxidation step. We used wet etching to remove the SiO₂ by using buffered oxide etch (BOE: 6:1 volume ratio of 40% NH₄F in water to 49% hydrofluoric acid (HF) in water). To

avoid the whole NW being thermally oxidized, we used dry thermal oxidation rather than the wet oxidation. Since the wet oxidation rate is more than 10 times faster than the dry oxidation rate, dry oxidation is more controllable for thinning small USNWs, while wet thermal oxidation may be suitable for thick microwire thermal oxide growth and the creation of a smooth interface at the oxide/Si interface. We relied on measurements of the NW diameter after each oxidation and oxide stripping step with the SEM because deviations from the thermal oxidation rate calculated with Massoud Model^[1] were observed and as expected due to slow oxidation in NWs. We practically repeated the thermal oxidation and wet etching for a few times to get the USNW as sharp as a few nanometers of tip diameter (Figure S1m-o). The process is repeatable and shows 100% yield (visual inspection of the USNWs' tip condition via SEM) of all samples as two examples shown in Figure S2a-h.

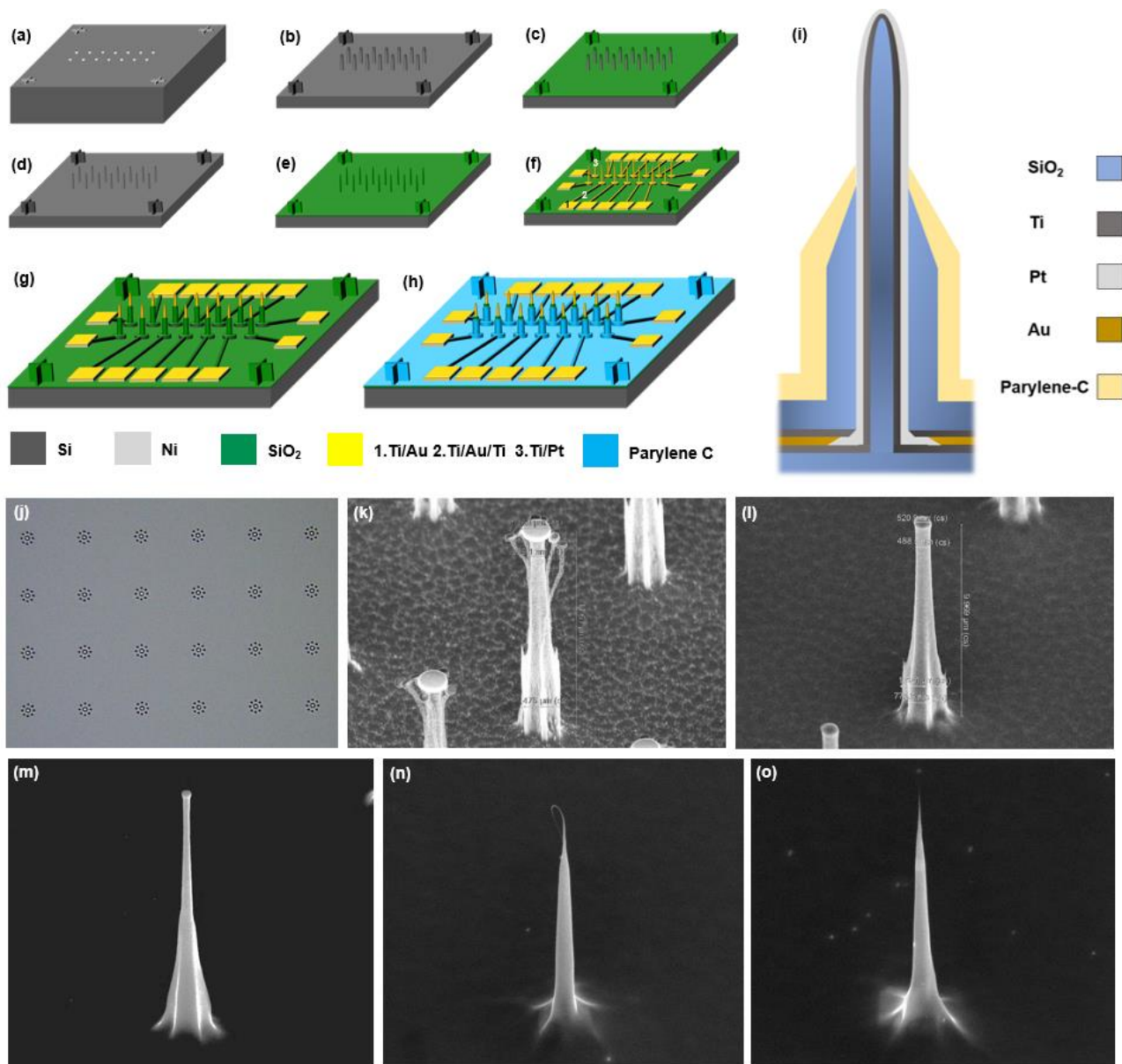


Figure S1. Overview of the fabrication process with a) Patterning Ni dots on Si substrate, b) Dry etching micro/nanowires, c) Thermal oxidation, d) Wet etching of oxidation layer, e) Thermal oxidation, f) Definition of the metal leads and contacts by electron-beam and photolithography, and g) 500 nm PECVD SiO₂ passivation h) 500 nm parylene C passivation and selective removal at the NW tip. i) Cross-section overview of the fabricated USNW. j) Top-view optical microscope (OM) image of patterned Ni dot arrays for Si NW etching. The center dot diameter was 800 nm. The peripheral dot diameter was 300 nm. k) SEM image of as-etched Si NWs showing thin peripheral NWs, mostly collapsed and a central NW with narrower tip than its base. l) After Ni mask etching, the NW was subjected to the first oxidation and BOE etching. The tip diameter was 200 nm and the NW length was ~10 μm. m-o) Sequential oxidation and oxide

stripping leading to (1) smoothening of the NW surface, (2) reduction of its diameter to sub-10 nm, and (3) reduction of its height to $\sim 6.5 \mu\text{m}$. The final NW is fully oxidized.

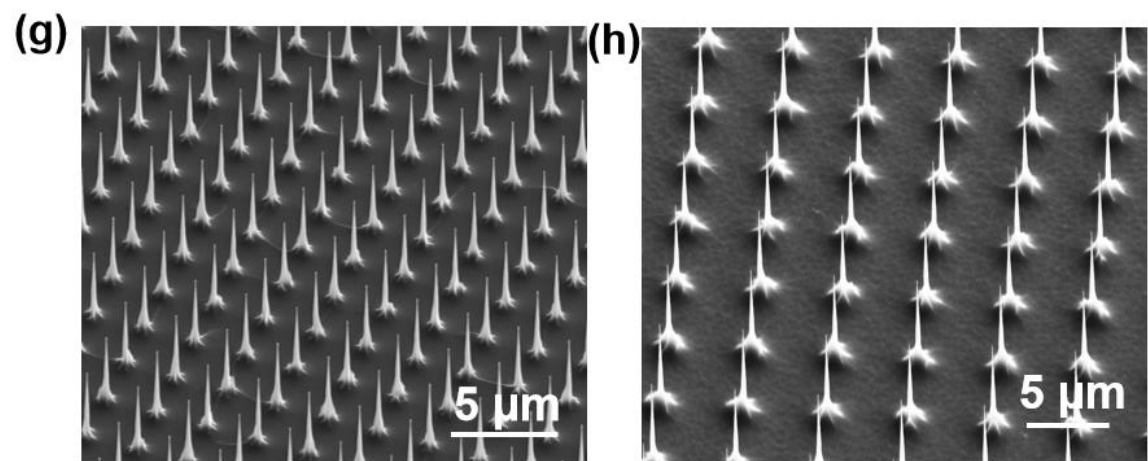
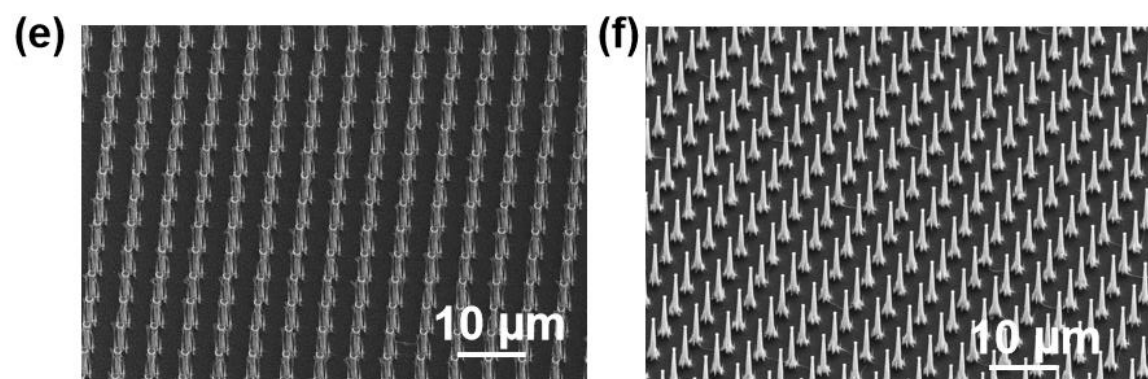
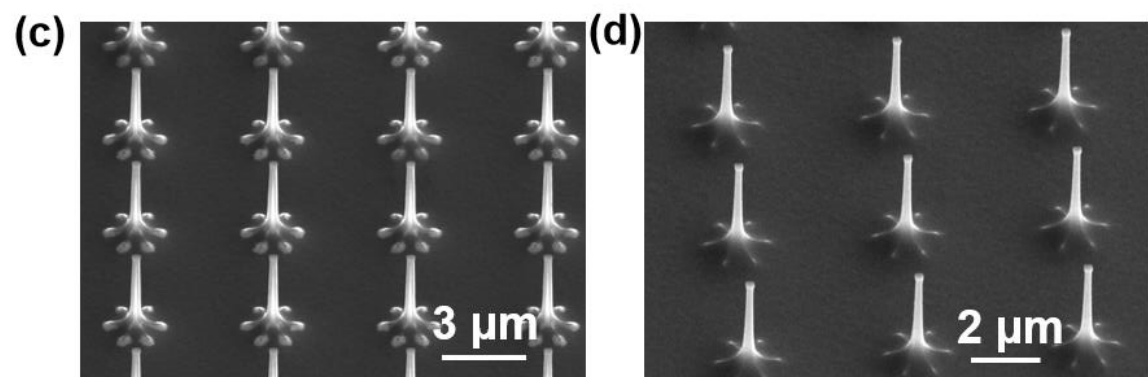
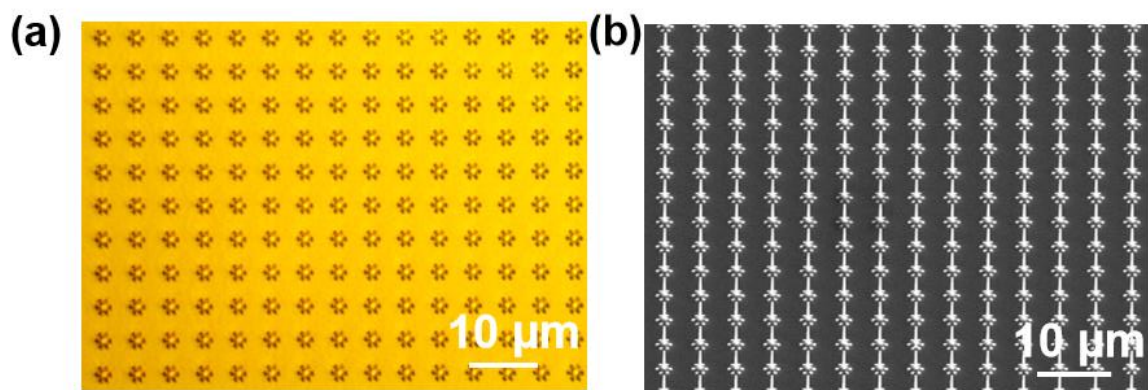


Figure S2. a) Top-view OM image of patterned Ni dot arrays for Si NW etching. The center dot diameter was 800 nm. The peripheral dot diameter was 300 nm. b-d) SEM images of an example that shows sequential oxidation and oxide stripping leading to reduced diameter of the NWs in the array, smoothing of the NW surface and the tapered structure. e-h) SEM images of another example that shows dry etching, sequential oxidation and oxide stripping leading to smoothing of the surface of the NWs in the array and the reduction of their diameter to sub-10 nm.

1.2 Fabrication for electrodes and metal interconnects

We performed a final step of 400 nm thermal oxide growth on the surface after the NW tip reaches a few nanometers. After the sample cleaning by acetone airbrush, rinsing by isopropyl alcohol (IPA), drying by N₂, dehydration at 180 °C on a hot plate, O₂ plasma at 200 W for 1 min, we spun coated a layer of electron beam resist (950 PMMA A6) with spin-coating condition of 4000 rpm, 500 rpm s⁻¹ and 40 s, and baked the sample at 170 °C for 10 min. Then, we used EBL to write the pattern with the dosage of 1800 μC cm⁻² for metal leads and 3000 μC cm⁻² for dots (aligned with the USNW) under the electron beam condition at 100 kV and 6 nA, followed by development (methyl isobutyl ketone (MIBK):IPA = 1:3) at 0 °C for 2 min, which opens the electron beam resist (950 PMMA A6) on the surface of the USNWs to connect to the metal leads. We used O₂ plasma for removal of 3-5 nm-thick PMMA residue on the pattern at 100 W for 1 min. A conductive layer, e.g. 10 nm Ti / 100 nm Au or Pt, etc., was uniformly coated on the sidewall of the USNW to form a conductive layer and connect the electrode tip to the metal leads (Figure S3a,d,e). Then, photolithography was used to pattern the outer large electrodes and interface/probing pads (Figure S3b). Finally, we used plasma enhanced chemical vapor deposition (PECVD) to deposit a layer of 300 nm SiO₂ at 350 °C (for first experiment) on the surface of the device with a hard mask (Si wafer with a pocket opening in the center) to avoid the SiO₂ deposition on the around the interface/probing pad (Figure S3c). Then, we spin-coated a layer of electron beam resist (PMMA 950 A4). After 10 min of hard bake at 170 °C, 10 – 20 s of O₂ plasma with 200 W was applied to clean the thin PMMA layer on the tip of the USNW. Then,

we used BOE to etch the SiO₂ on the tip. After cleaning PMMA by acetone and O₂ plasma, the USNW has ultra-sharp tip (~30 nm) is shown in (Figure S3f). The sample with 128 channels of individually addressable USNWs are distributed for 4 arrays with different USNW pitch as 5 μm, 10 μm, 30 μm, 70 μm as shown in the Figure S4a-d, respectively. The process also enables variable USNW height as an example shown the USNW electrode with height of 2.9 μm to 9 μm in Figure S4e-i.

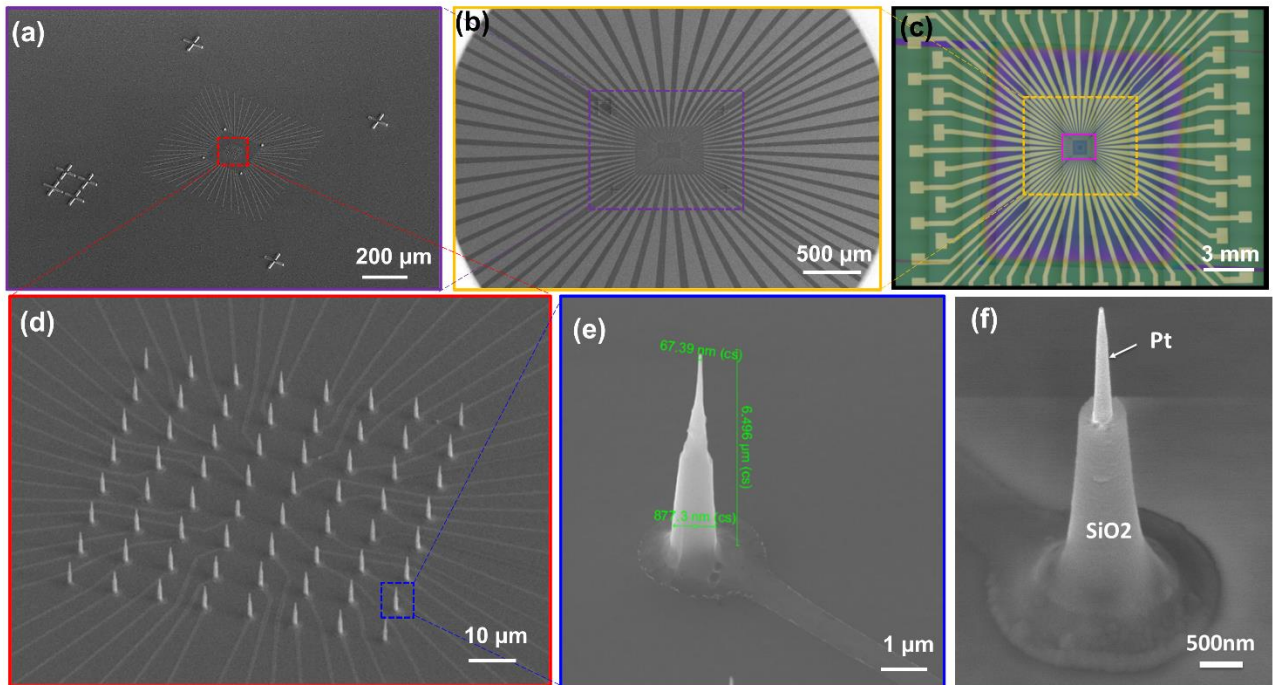
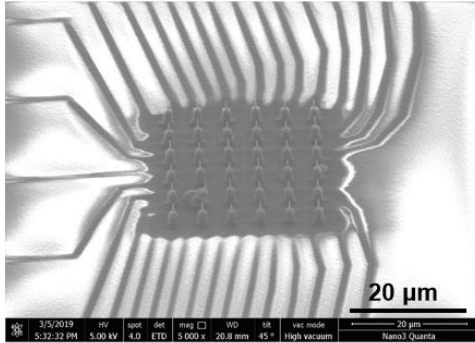


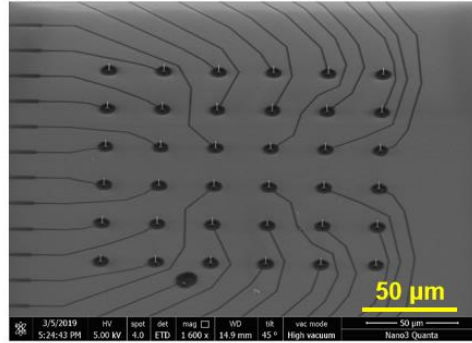
Figure S3. Metallization and Passivation of USNW and Electrode. a) SEM image of the e-beam lithography patterned portion of the USNW array, where metal lead extensions were contained within the e-beam lithography patterned alignment marks within the e-beam lithography writing field. b) SEM image of the device after the photolithography patterning and deposition of the extension metal leads to the interface/probing pads. c) Optical image of the device with passivation surface of SiO₂ deposited by PECVD. d) Zoom-in images of the USNW array in a). e) SEM image of a single USNW coated with a thin (30 nm) Pt layer conformally deposited by e-beam evaporation. f) USNW with passivation of its base by PECVD deposited SiO₂.

Fixed NW height (6.5 μm), variable pitch:

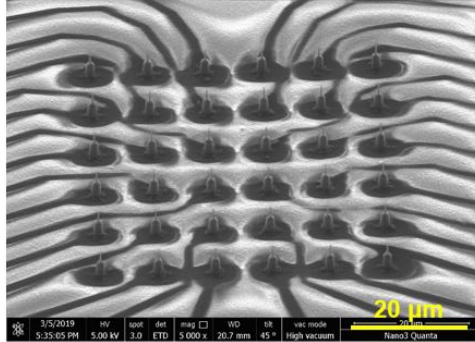
(a) 5 μm pitch



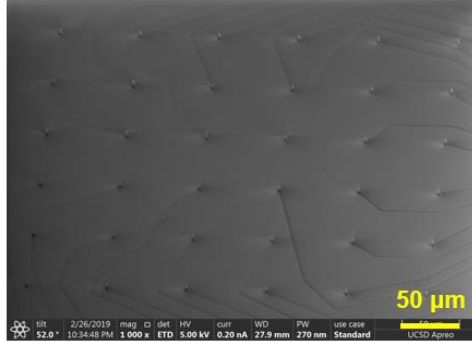
(b) 10 μm pitch



(c) 30 μm pitch

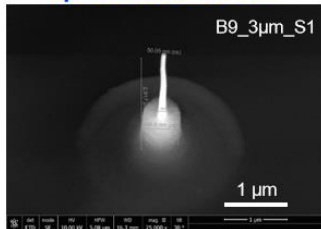


(d) 70 μm pitch

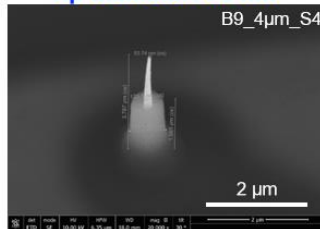


Fixed pitch (10 μm), multiple nanowire heights:

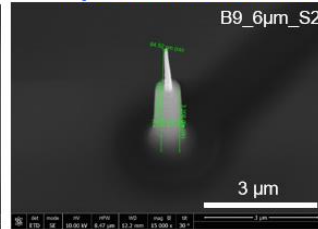
(e) NW height: 2.9 μm
Tip diameter: 50 nm



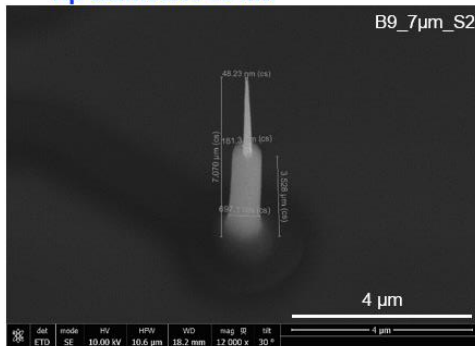
(f) NW height: 3.7 μm
Tip diameter: 54 nm



(g) NW height: 5.5 μm
Tip diameter: 64.5 nm



(h) NW height: 7.1 μm
Tip diameter: 48 nm



(i) NW height: 9 μm
Tip diameter: 48 nm

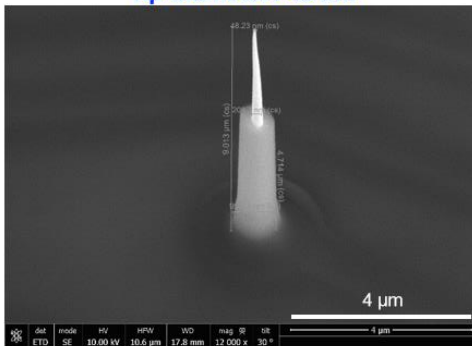


Figure S4. a-d) SEM image of the vertical USNW device arrays. Each device consisted of 128 USNWs in total, and 4 arrays, each with 32 USNWs and different pitch as labeled in a-d) (groups A to D). The 4 USNWs at each corner are not connected to the metal leads. e-i) The process also enables fixed pitch and variable USNW height as shown in panels e-i.

1.3 Optimization of passivation

After culturing the cells on the devices for 14 days, a layer of 300 nm thick SiO₂ on Cr/Au metal leads peeled off as shown in Figure S5a. A FIB cross-section of the peeled-off region was cut and showed a gap between the SiO₂ and the metal lead (Au or Pt) (Figure S5b), because of the poor adhesion between SiO₂ with the noble metals. Another problem was that the leads patterned by electron beam lithography (EBL) had tall edge beads (Figure S5c) because the conformally electron beam deposited metal caused difficulty of the lift-off at the edge of the pattern. To solve the peel-off problem, we deposited an adhesion layer of metal (10 nm Ti) on top of the previous Au or Pt, which enhanced the adhesion between passivation and the metal layers. Then, during EBL of the center leads, we also changed the electron beam resist from a single layer of e-beam resist (PMMA 950 A6) to double layers of resists (Methyl methacrylate (MMA) (8.5) A6 and PMMA 950 A6). The usage for MMA/PMMA bilayer in EBL helps lift-off of metallic structures, since MMA/PMMA bilayer gives an undercut resist profile to avoid metal coating on the sidewall of the resist during the electron beam deposition. We also increased the thickness of the SiO₂ passivation layer to 500 nm. After these steps of modification, we did an accelerated aging test of the devices by submerging them in saline solution at 60 °C for 3 days, which is equivalent to the condition of 37 °C for 15 days (cell culture temperature and timeline). The devices showed clear surface (Figure S5d) after the aging test. Two cross-sections of FIB-SEM images demonstrated good adhesion between metal and passivation layer (Figure S5e) and no edge beads (Figure S5f).

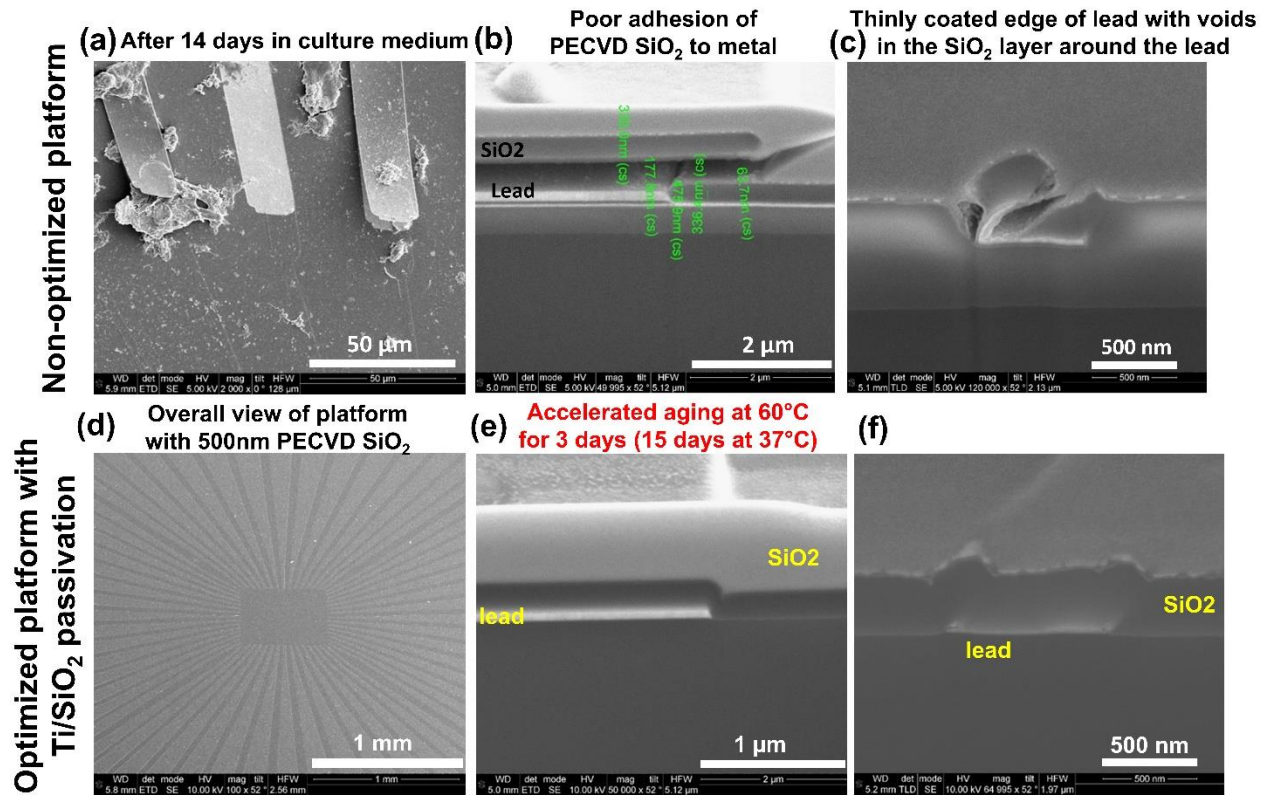


Figure S5. a-c) 300 nm PECVD SiO₂ passivation layer on top Cr/Au metal leads show gross delamination in panel (a) and local delamination in panel (b) after 14 days *in vitro* culture. Gaps in the SiO₂ PECVD layer around the edges of the metal leads are also observed in panel (c), SEM image of a device with dual SiO₂/parylene C passivation. d–f) To increase adhesion with the top PECVD passivation layer, we added a 10 nm thin Ti layer on top of the Au metal leads. We also increased the thickness of the SiO₂ passivation layer to 500 nm. e–f) With these modifications, accelerated aging in DPBS solution at 60 °C demonstrated intact platform.

1.4 Surface roughness optimization

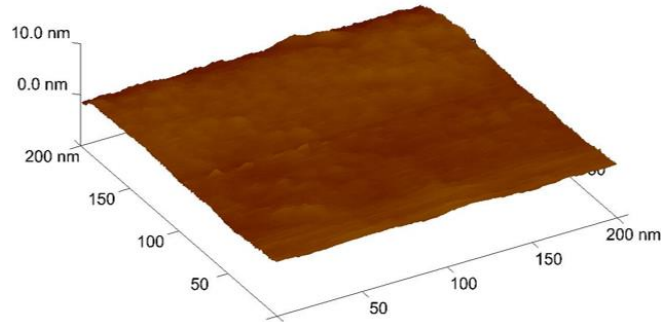
The USNW array devices were fabricated on the prime-grade Si substrate, and the surface of the devices (thermally grown SiO₂) showing a rms surface roughness less than 1 nm in the atomic force microscopy (AFM) topography image (Figure S6a). Since the surface roughness influences the cell's attachment and neurite formation, we optimized the surface roughness by two methods in Figure S6b,c. To create a rough surface on our device, we employed diluted HF (volume ratio of HF:DI water = 1:10) since it does not etch the surface SiO₂ uniformly. Our

device had two types of SiO₂: the first layer is a thermally grown SiO₂ while second layer is PECVD grown SiO₂. First, we used diluted HF to etch the device with as-thermally grown 200 nm SiO₂ and the surface roughness was characterized by AFM (Figure S6b). The 30 s etching produced 2.22 nm average roughness and 20.26 nm maximum roughness; the 60 s etching created 1.83 nm average roughness and 15.20 nm maximum roughness; the 90 s etching created 0.37 nm average roughness and 4.29 nm maximum roughness. Then, we used diluted HF to etch the device with 500 nm SiO₂ deposited by PECVD and the surface roughness was characterized by AFM (Figure S6b). The 30 s etching produced 1.12 nm average roughness and 15.62 nm maximum roughness; the 60 s etching created 4.34 nm average roughness and 50.71 nm maximum roughness; the 90 s etching created 12.2 nm average roughness and 147.03 nm maximum roughness.

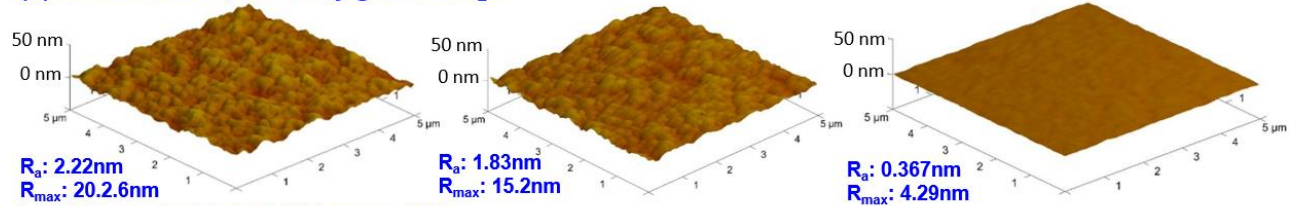
Earlier studies have shown that parylene C is a bio-compatible organic polymer material,^[2] and parylene C with high nanoscale surface roughness and stable hydrophilic surface is good for protein attachment that helps cell adherence after plasma treatment.^[3] We used parylene C as a top layer on our devices to preserve the cell's health during culture on our platform. 500 nm parylene C was deposited by SCS PDS 2010 Specialty Parylene Coating System. Then, we spin-coated a layer of positive photoresist (AZ 1518), applied a hollow polydimethylsiloxane (PDMS) mask with Al foil to protect the center parylene C layer and the USNW array during exposure step of the photolithography, followed by developing with AZ 300 MIF developer. The exposed parylene C at the pad regions and USNW tips were etched by O₂ plasma in Oxford P80 RIE etcher while the remaining part was protected by photoresist AZ 1518; after tip exposure, the passivating AZ1518 was removed. The final SEM image of the USNW

with two passivation layers is shown in Figure S7a. We also used AFM to characterize the surface roughness, which showed an average roughness of 7 nm in Figure S7b.

(a) Starting Thermal SiO₂ surface $R_a < 1\text{ nm}$



(b) HF based etch, thermally grown SiO₂:



(c) HF based etch, PECVD grown SiO₂:

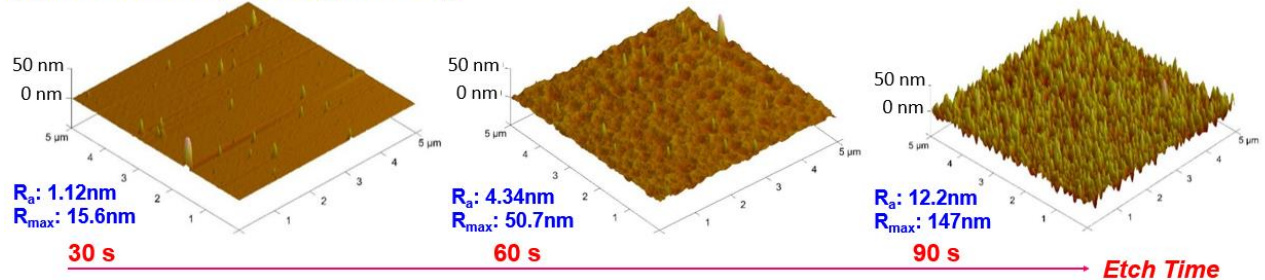


Figure S6. a) Atomic force microscopy (AFM) topography images of the surface of the devices (thermally grown SiO₂) showing a rms surface roughness less than 1 nm. PECVD deposited SiO₂ also exhibited a similar rms surface roughness. b) We used diluted HF treatment to roughen the surface to promote neuronal adhesion to the surface of the device. We observed that with the etching time increase, the rms surface roughness decreases. c) For PECVD grown SiO₂, the surface roughness increased with time. In our experiments, we used samples with rms surface roughness of 2 - 5 nm.

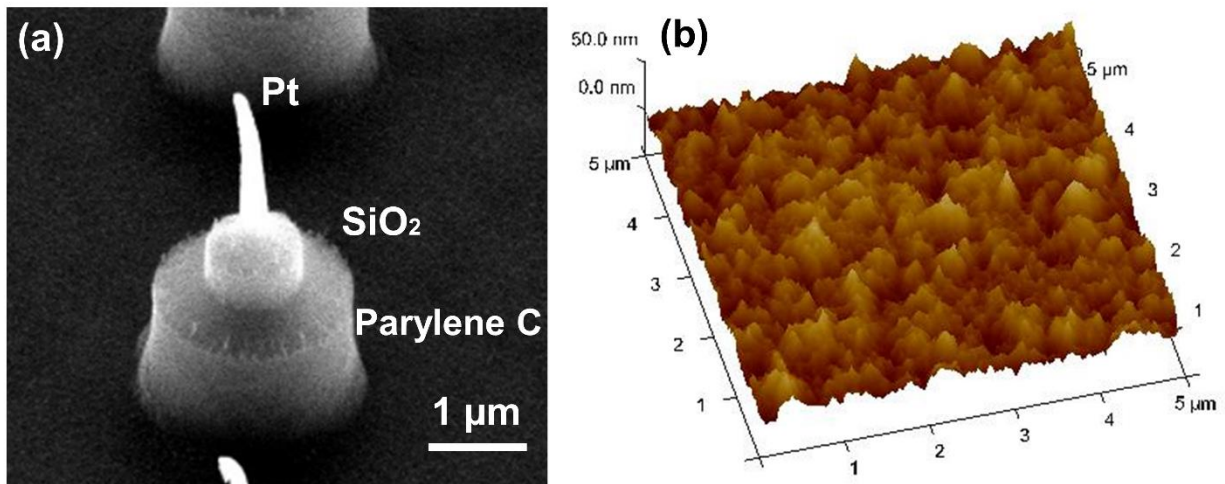


Figure S7. a) SEM image of a device with dual SiO₂/parylene C passivation. b) AFM image of dual SiO₂/parylene C passivated surface. We performed O₂ plasma treatment to roughen the surface of the parylene C, similar to the SiO₂ surfaces. The resulting rms surface roughness was 7 nm.

1.5 Packaging of the USNW array device and FFC bonding

Following fabrication, passivation and surface roughening, we bonded a culture chamber ring in the center of the devices using custom-made PDMS for sealing, where cells were cultured inside of the chamber. Then, the device was bonded with the flexible flat cable (FFC) by using the anisotropic conductive film (ACF) bonding at 100 °C (Figure S8).

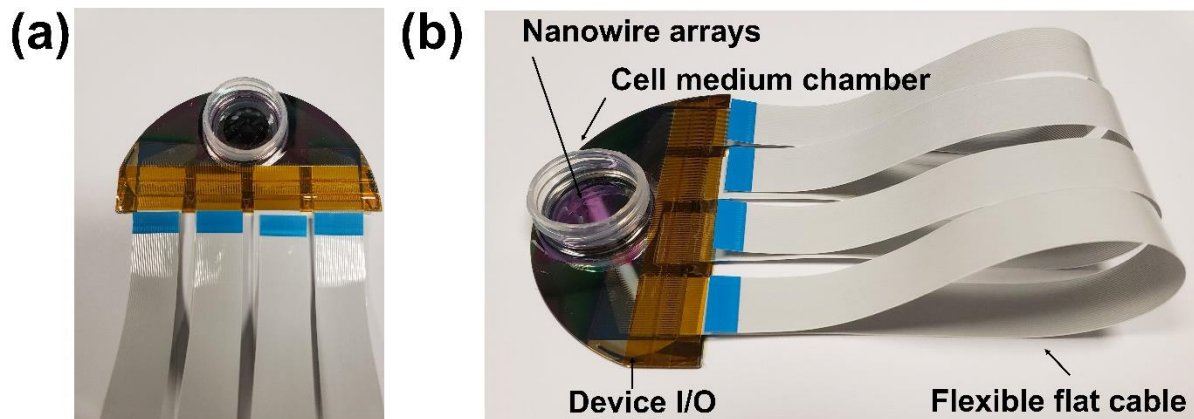


Figure S8. a-b) Picture of a completed device with a custom-made PDMS-sealed culture chamber and ACF bonding of FFC (6'' long). The culture ring is adhered to the parylene C/ PECVD SiO₂/ thermal oxidation SiO₂/ Si-substrate surface with PDMS. The open central area for cell culture has an approximate diameter of 7 mm.

2. Electrochemical characterizations of individually electrically addressable Si USNW array devices

2.1 1 kHz electrochemical impedance assessment across arrays

The 1 kHz electrochemical impedance of the 128 channels of the USNW array devices was measured by the Intan RHS2000 Stimulation/Recording System by using a Pt wire as a counter electrode and soaking in the Dulbecco's phosphate-buffered saline (DPBS) solution. A representative of the 128 channel devices shows 100% yield based on impedance measurements (Figure S9a) and an average 1kHz impedance of $15.2 \pm 0.3 \text{ M}\Omega$, with four arrays' average 1kHz impedance of $14.4 \pm 0.5 \text{ M}\Omega$, $11.6 \pm 0.2 \text{ M}\Omega$, $17.4 \pm 0.6 \text{ M}\Omega$, $16.4 \pm 0.6 \text{ M}\Omega$, respectively.

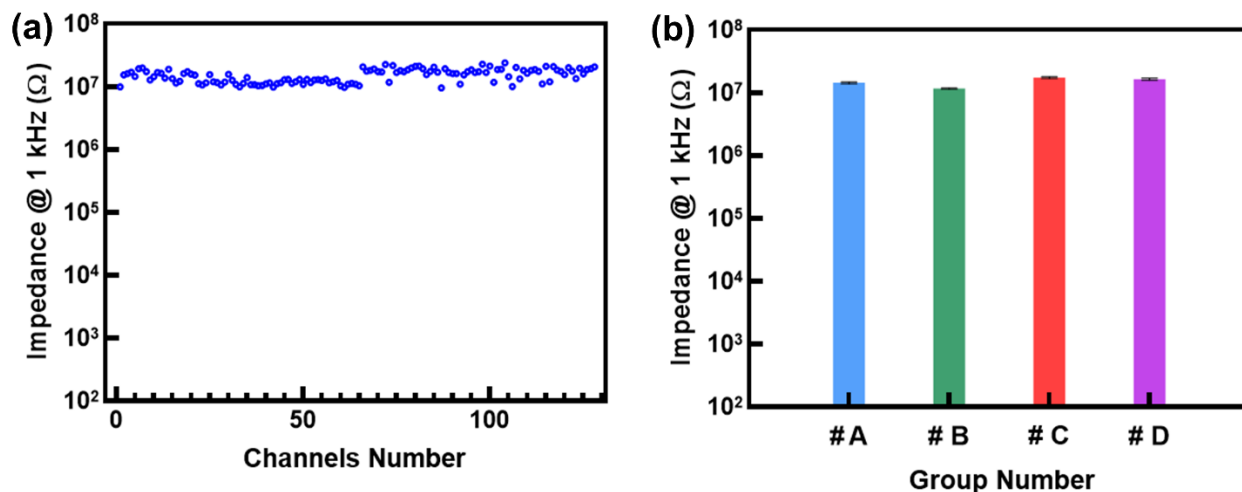


Figure S9. **a)** Electrochemical impedance of the 128 channels of individual USNW array at 1 kHz. **b)** Average electrochemical impedance at 1 kHz of each of 32 channels of individual USNW array in groups A, B, C, and D (14.4 ± 0.5 M Ω , 11.6 ± 0.2 M Ω , 17.4 ± 0.6 M Ω , 16.4 ± 0.6 M Ω , respectively).

2.2 Electrochemical impedance spectroscopy and charge injection capacity

To improve the electrical stimulation efficiency, we electroplated poly(3, 4-ethylenedioxythiophene):poly(styrenesulfonate) (PEDOT:PSS) on the stimulation channels of the array (Figure S10), since PEDOT:PSS allows higher current injection than the bare electrode. Next, electrochemical impedance spectroscopy (EIS) was performed by using the GAMRY Interface 1000E with merging the USNW array in DPBS solution and using the three electrode setup^[2]: a large Pt electrode as a counter electrode, an Ag/AgCl electrode as a reference electrode, and USNW with electroplated PEDOT:PSS as the working electrode. Then, sinusoidal signals with 10 mV rms (root mean square) AC voltage (zero DC voltage) were applied. We measured the electrochemical impedance for a bare USNW (Figure S11a) and a USNW with electroplated PEDOT:PSS (Figure S11b) with the frequency range from 1 Hz to 10 kHz. The electrode impedance decreased by 50 times.

In addition, electrochemical current pulse injection with chronopotentiometry mode was performed by using the GAMRY Interface 1000E by submerging the USNW array in DPBS solution and using three electrodes setup: a large Pt electrode as a counter electrode, an Ag/AgCl electrode as a reference electrode, and USNW or USNW with electroplated PEDOT:PSS as the working electrode. Cathodic first, bi-phasic, charge-balanced current pulse was injected across the counter electrode and the working electrode, while the working electrode's polarization potential with reference to Ag/AgCl reference electrode was measured. E_{mc} was calculated as working electrode potential versus Ag/AgCl reference electrode 10 μ s after cathodal pulse phase, while E_{ma} was calculated as working electrode potential versus Ag/AgCl electrode 10 μ s after anodal pulse phase. For organic electrodes (PEDOT:PSS/Au or PEDOT:PSS/Pt), the water window limit is between -0.9 V to 0.6 V; while for metallic electrodes (Pt or Au), water window limit is between -0.6 V to 0.8 V.^[4] E_{mc} is the potential when the electrode/solution interfacial potential reaches reduction (cathodal limit) and E_{ma} is the potential when it reaches oxidation (anodal limit). Charge injection capacity (CIC) is the total charge density at which either E_{ma} reaches water oxidation potential or E_{mc} reaches water reduction potential expressed by $CIC=Q_{inj}/GSA$ (geometric surface area). The CIC for bare Pt USNW and the USNW with electroplated PEDOT:PSS were 0.60 mC cm⁻² and 2.98 mC cm⁻², respectively (Figure S11c,d). Electroplating PEDOT:PSS on the USNW increases its current injection capacity by nearly 5 times. The PEDOT:PSS is therefore more effective for neuronal stimulation to avoid reaching water hydrolysis.

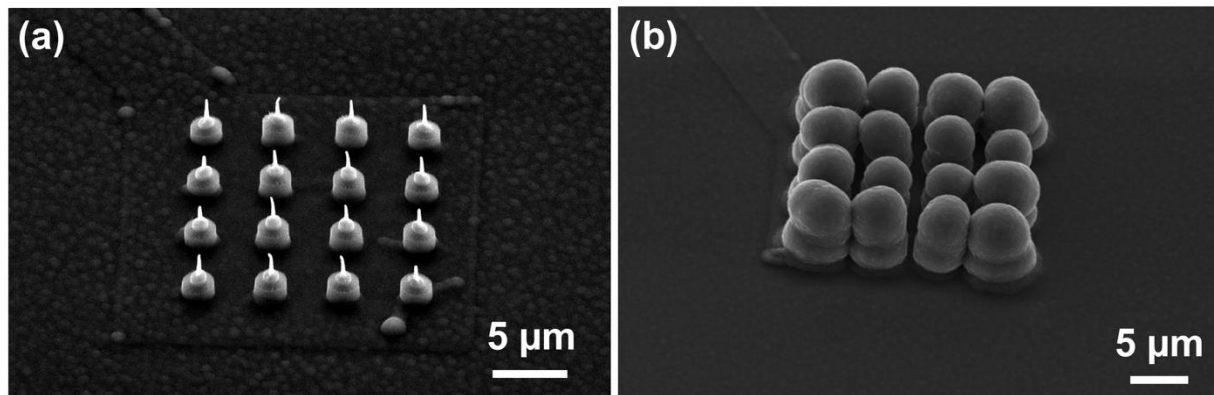


Figure S10. a-b) SEM image of a pad with 16 NWs (a) before and (b) after PEDOT:PSS electroplating.

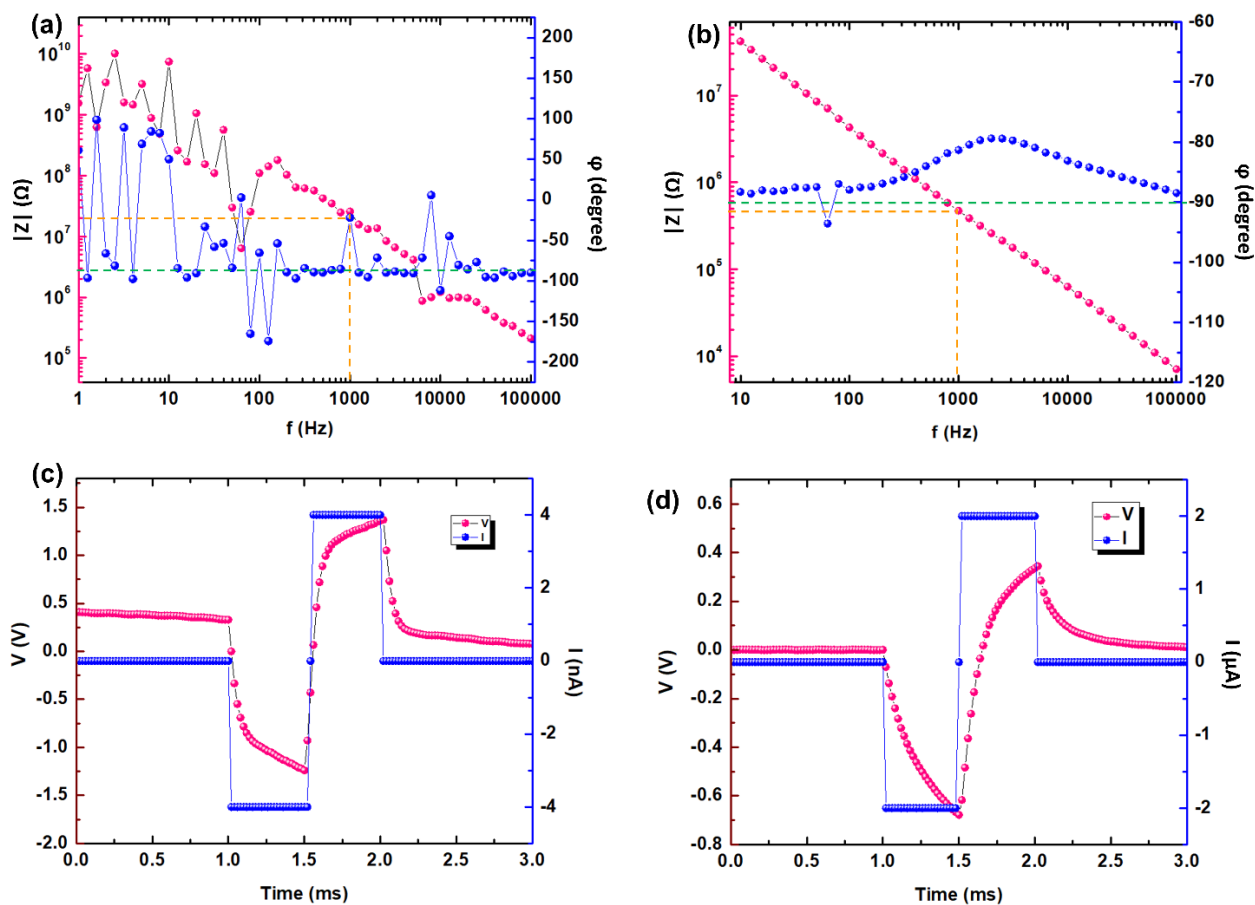


Figure S11. a-b) Impedance spectroscopy for (a) 16 NWs with bare Pt NW surface and (b) after PEDOT:PSS electroplating, showing lowered impedance by ~ 50 times. c-d) Voltage transients at the water hydrolysis window for bare NW with Pt surface (c) showing a maximum current capability of 0.60 mC cm^{-2} and (d) after PEDOT:PSS electroplating showing a maximum current capability of and 2.98 mC cm^{-2} before breaking water.

3. Cell culture

3.1 Rat cortical neuron culture on USNW array devices

The integration of USNW array electrodes with cells followed immediately from fabrications and packages of the device, which involved the following steps (steps 1 to 4 were also applied before iPSC-CVPCs cultures):

(1) The USNW array device was sterilized by 1) DI water rinse for three times, and 2) 70% ethanol for at least 30 min.

(2) The device was washed with PBS for three times followed by placing 20 μl (0.1% w/v) Polyethylenimine (PEI, Sigma-Aldrich) solution on the USNW array and incubating them at 37 °C incubator for 1 hour.

(3) The PEI was aspirated and washed with 500 μl double distilled water (ddH₂O) for 4 times. The device dried in the incubator for 5 hours or overnight.

(4) 20 μl laminin (20 $\mu\text{g ml}^{-1}$, Sigma-Aldrich) was added to the USNW array spot and incubated at 37 °C incubator for 1 hour.

(5) Medium (Neurobasal (Thermo Fisher Scientific) +2% B27 (Thermo Fisher Scientific) +1% P/S (Corning) + 10% FBS) was prepared for plating rat cortical neurons (RCNs) on USNW arrays.

(6) The cryopreserved rat neurons cryovial (from Thermo Fisher Scientific) was removed from the liquid nitrogen storage container, warmed in a 37 °C water bath for exactly 2.5 min, sprayed the outside with 70% ethanol, wiped dry, and placed in a bio-safety cabinet.

(7) The contents of the cryovial were carefully transferred to a 15 mL centrifuge tube using a 1 mL pipettor. The inside of the cryovial was carefully washed with 1 mL of room temperature Neurobasal medium ($\sim 1 \text{ drop s}^{-1}$). 3 mL of room temperature Neurobasal medium was slowly

added to the tube ($\sim 1-2$ drops s^{-1}). The contents were carefully mixed by inverting the tube 2-3 times. The total number of cells in suspension was determined via hemocytometer count.

(8) The cells were concentrated by centrifuging 1100 rpm for 3 min. Laminin was aspirated and 20 μ l cell suspension was plated directly on the USNW arrays with the cell density at 200k cells/array. The USNW devices with seeded neurons were incubated in a cell culture incubator at 37 °C, 5% CO₂ for 35-40 min. Next, 500 μ L of warm Neurobasal medium was carefully added to chamber from the side of the device. To avoid adding the medium too fast to cause the detachment of the adhered neurons on the USNWs, the USNW devices with seeded neurons were put back to the cell culture incubator at 37 °C, 5% CO₂ for another 35-40 min. Then, another 500 μ L of warm Neurobasal medium was carefully added to chamber from the side of the device to reach a volume of 1.5 mL per device.

(9) On the next day, the medium was changed to Brainphys Complete (Stem cell) + supplements (brain-derived neurotrophic factor (BDNF), glial cell line-derived neurotrophic factor (GDNF), Ascorbic acid, cyclic adenosine monophosphate (cAMP) and Laminin). Then, half the medium was replaced with fresh medium for every other day with Brainphys + supplements till 7 days *in vitro* (DIV), then switched back to Brainphys Complete with no added supplements. This showed clear neuronal network formation on the USNW array platform (Figure S12).

In parallel to plating on USNW array devices, rat cortical neurons were also plated at a density of 20,000 cells/well in (Neurobasal (Thermo Fisher Scientific) +2% B27 (Thermo Fisher Scientific) +1% P/S (Corning) + 10% FBS) on 384 well imaging plates (Poly-D-lysine treated, Biocoat, Corning), which had been pre-coated with laminin (20 μ l/well) for 1h at 37°C. Cells were maintained in a humidified 37°C incubator with 5% CO₂, with media exchanges into BrainPhys that exactly paralleled those described above for culture on USNW array devices.

Rat cortical neuronal cultures on 384-well imaging plates were fixed in 4% paraformaldehyde (PFA) (Alfa Aesar Chemicals) for 10 min at room temperature at 2 and 4 weeks after plating. The cells were then washed 3 times in phosphate buffered saline (PBS) (Gibco|Thermo-Fisher Scientific), and then blocked in 5% donkey serum (Jackson ImmunoResearch) and permeabilized in 0.1% Triton-X (Sigma-Aldrich) in PBS. Primary antibodies at the dilutions noted (Table 1) were incubated on the cells overnight at 4°C. The following day cells were washed 3 times in PBS, and the secondary antibodies (AlexaFluor, Molecular Probes) were added 1:500 in blocking buffer for 2 hours at room temperature. The secondary antibody was then washed several times in PBS and DAPI (Thermofisher, 1:2000 in PBS) was added for 30 min at room temperature. Images were acquired with the Opera Phenix High Content Screening System confocal microscope (Perkin Elmer).

Antibody	Species	Dilution	Company
GFAP	Goat	1:500	Santa Cruz Biotechnologies
MAP2	Guinea Pig	1:1000	Synaptic Systems
Tuj1	Mouse	1:500	Biolegend

Table S1. Antibodies Specification.

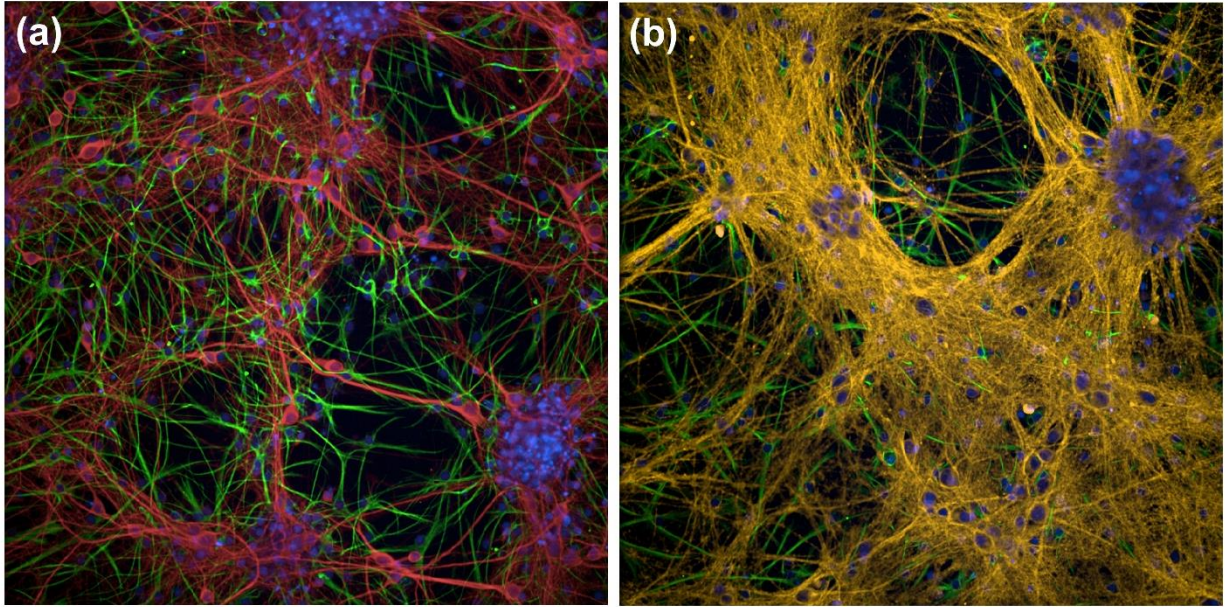


Figure S12. a-b) Fluorescence images of rat cortical neurons (a) Red: MAP2b neuronal marker; Green: GFAP, astrocyte marker; Blue: DAPI nuclear marker. (b) Yellow: β -Tubulin, neuronal marker; Green: GFAP, astrocyte marker; Blue: DAPI nuclear marker.

3.2 iPSC-CVPCs culture on USNW array devices

iPSC-derived cardiovascular progenitor cells (iPSC-CVPCs) were derived and cryopreserved at day 25 (D25) of differentiation.^[5-6] The cryopreserved iPSC-CVPCs were thawed either on a 6-well plate coated overnight with Matrigel (Corning) or directly on a USNW device coated with Matrigel for 5 hours or overnight. The following day, the medium was changed with fresh iPSC-CVPC medium (RPMI 1640 (Thermo Fisher Scientific) containing B27 Supplement (50X) (Thermo Fisher Scientific) and Pen-Step (Thermo Fisher Scientific)). When the iPSC-CVPC were thawed onto a 6-well plate, the cells were cultured for 2 days before plating on a USNW device. 5×10^4 , 1×10^5 or 2×10^5 cells were plated over the active regions of a USNW device in 5 - 8 μ L of the iPSC-CVPC medium containing B27 Supplement and Pen-Step (Thermo Fisher Scientific). After cells were plated on a USNW device, iPSC-CVPCs were

cultured for 5 - 7 days prior to first recording with medium changed every other day. The day before recordings of iPSC-CVPCs, the medium was replaced with fresh iPSC-CVPC medium.

3.3 Pharmacological stimulation and inhibition

Pharmacological responses were assessed to validate the neuronal activities are of electrophysiological origin. Picrotoxin (PTX) is an equimolar mixture of two compounds, picrotoxinin (C₁₅H₁₆O₆; CAS# 17617-45-7) and picrotin (C₁₅H₁₈O₇; CAS# 21416-53-5). If neurons are under GABA_A receptor-mediated inhibition, PTX will stimulate neurons by relief of inhibition.^[7] Tetrodotoxin (TTX) is a sodium gate channel blocker which suppresses cell firing. We recorded the baseline activities of rat cortical neurons on 7 DIV in Figure 3r, which showed some action potentials on channel A003. Then, we added PTX to a final concentration of 33 nM to the culture medium, and the neuronal activity increased and generated high-frequency action potentials (Figure 3s). Next, TTX was added to a final concentration of 1 nM to the culture medium and we observed that the activity decreased until it disappeared (Figure 3t).

4. SEM and FIB-SEM imaging on neurophysiology platform

The USNW array devices with cells were fixed, dehydrated, critical point dried and coated with IrOx for SEM imaging. The fixative mediums were the mixes of distilled water, sodium cacodylate buffer (0.2 M, pH 7.4) and Glutaraldehyde solution (G58882-10X1ML, Grade I, 25% in H₂O) with the ratio of 4:5:1. We first melted Glutaraldehyde solution at 37 °C water bath, then these mediums were mixed together by using spinner of VORTEX-GENIE 2 for 3 mins. Firstly, the growth media was rinsed with PBS for three times. Subsequently, the samples had undergone a cell fixation protocol, in which a solution containing 2.5%

glutaraldehyde in 0.1 M cacodylate buffer at pH = 7.4 was added. The sample sat for 1 hour at room temperature and was then washed three times in PBS with leaving the sample in PBS solution for 5 min after each rinse. Buffer salts were rinsed off with three washes in distilled water, 5 min for each rinse. The samples were then subjected to a dehydration procedure in which they were serially dehydrated in 30, 50, 70, and 90% (10 min each) and three times with 100% ethanol. Following the dehydration procedure, the samples were dried in critical point dry (CPD) by using Autosamdri-815 for ~10-15 min. Finally, a 10 nm IrOx was sputtered on the surface of the sample by using Emitech K575X coater (5-7 s at 85 mA) for SEM imaging (Neurons: Figure S13 and Figure S14, iPSC-CVPCs s: Figure S17) and 100+ nm of Ti was deposited on samples for protection of the surface for FIB processing (Figure S15 and Figure S16).

Initial cortical rat neuronal culture results on roughened SiO₂ surface (14 DIV)

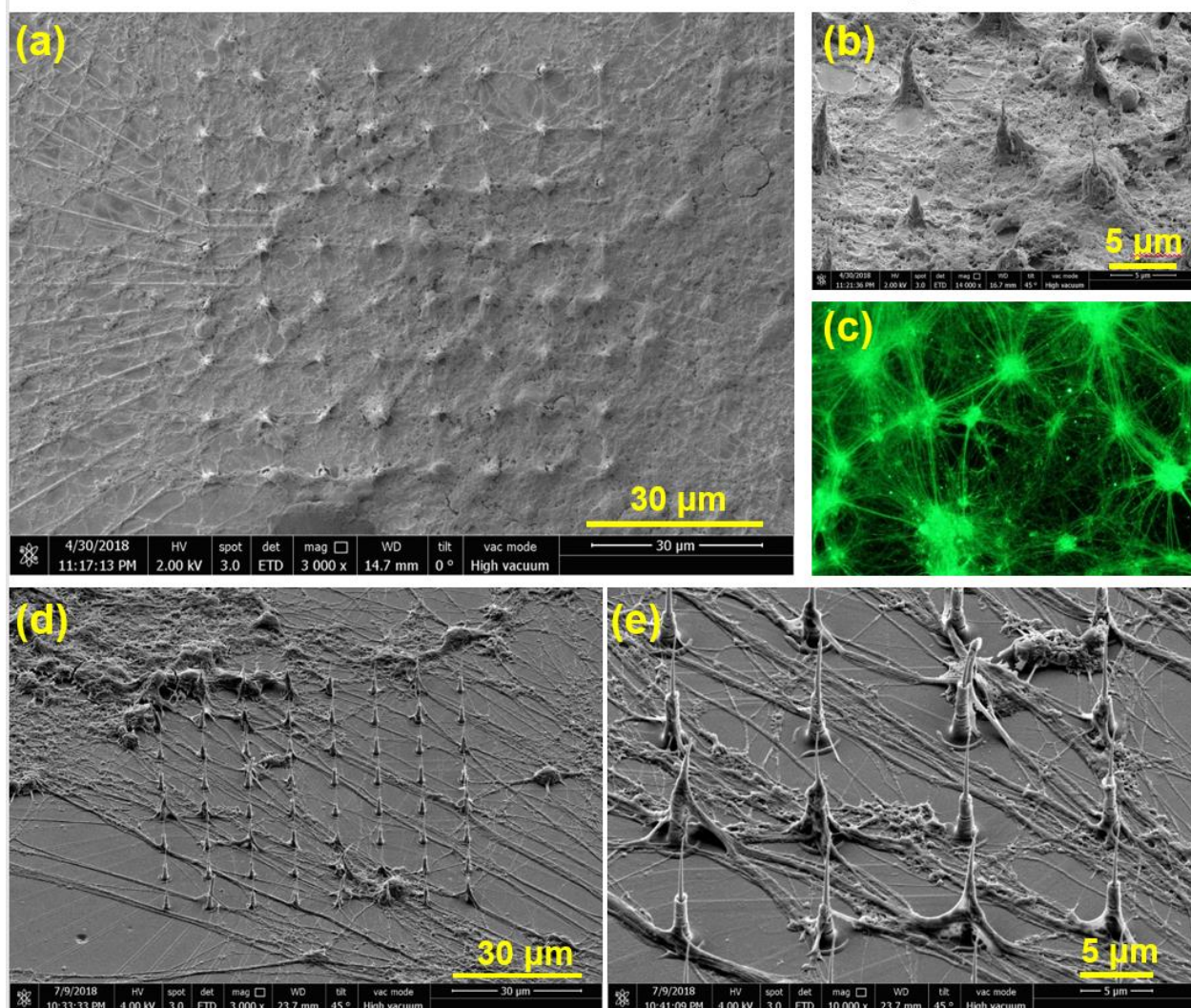


Figure S13. a, b, d, e) Top and angled view SEM images of cultured rat cortical neurons 14 days DIV on SiO₂-passivated USNW platform showing neurite extensions indicating healthy cell culture. c, Fluorescence imaging of the simultaneously cultured neurons on a control glass plate also demonstrating appropriate culture conditions. Total number of neurons was 200k for this experiment.

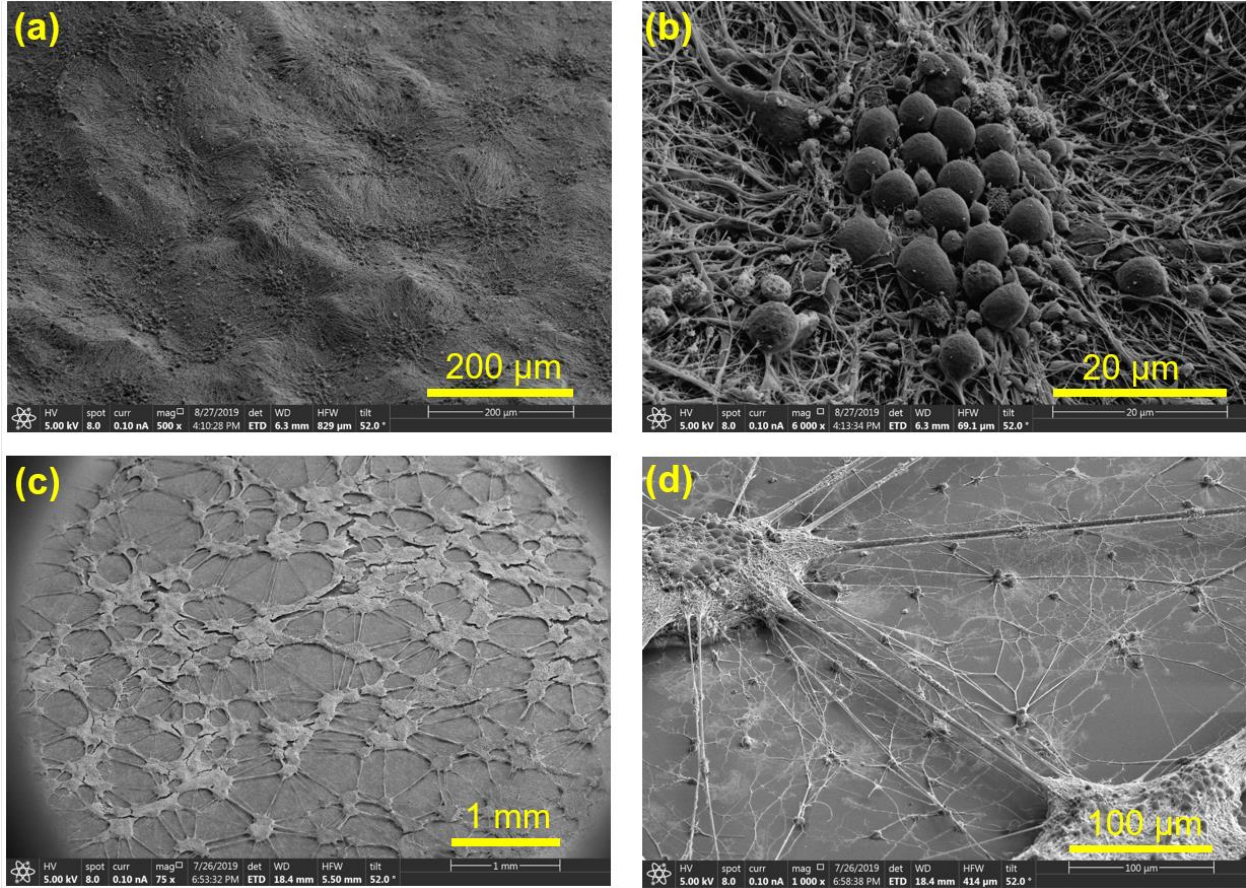


Figure S14. a-d) SEM images obtained from the cell culture on a single device. On certain portions of the device, we obtained continuous, tissue-like cell culture (a-b) as is further illustrated in Figure S8. In some other regions where no global clustering was observed, we obtained satellite-like clusters of 3D cultured layers (c-d). Total number of neurons was 800k for this experiment.

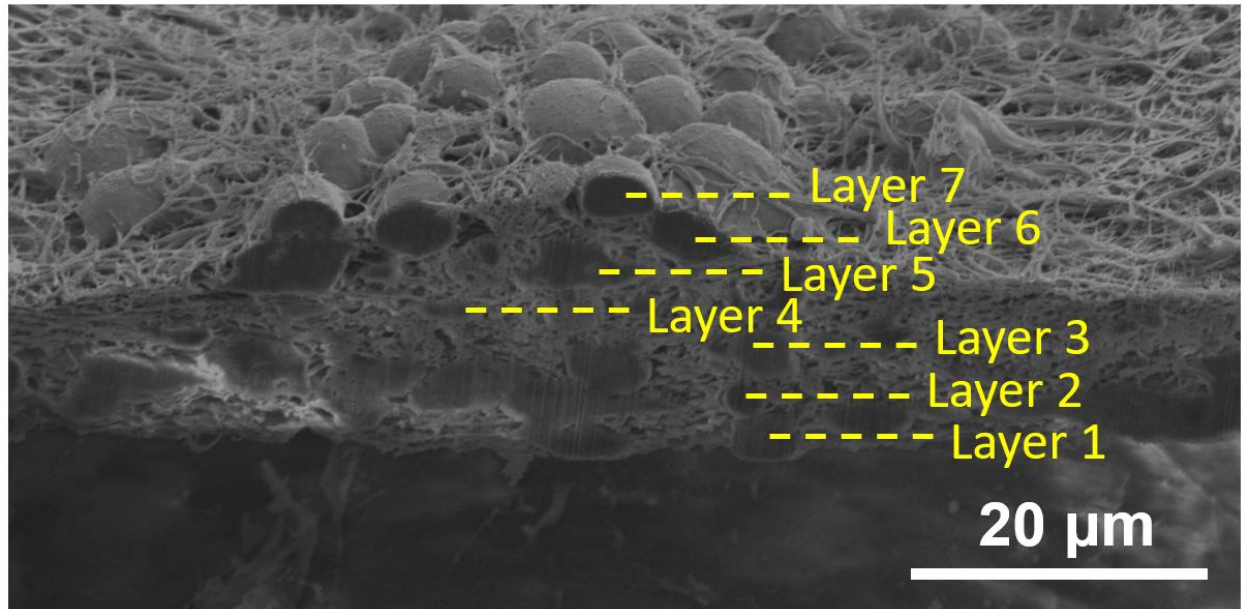


Figure S15. Original SEM image taken in the cross-section (sectioned by FIB) showing multi-layered neuronal structure.

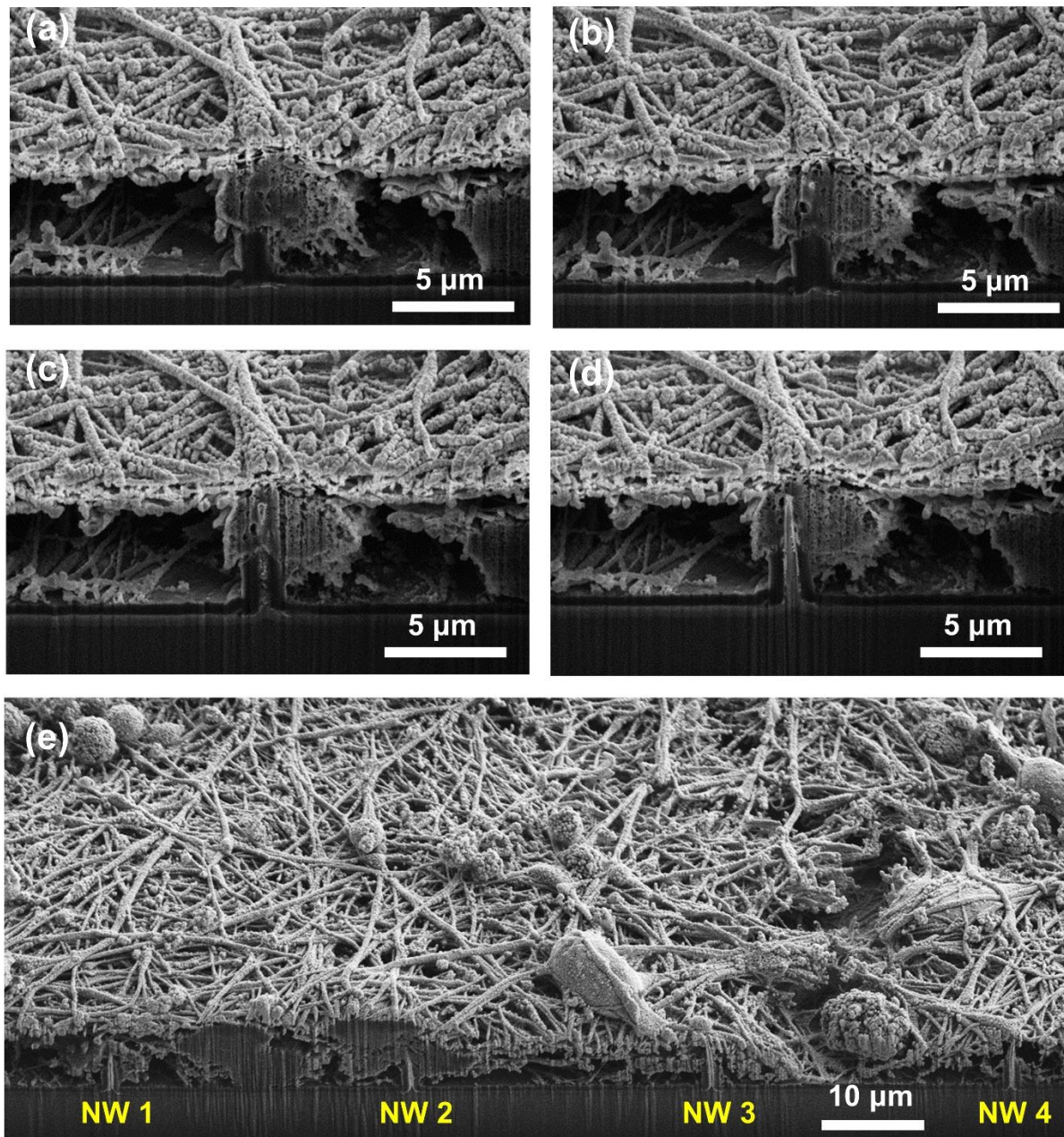


Figure S16. Original SEM image taken in the cross-section (sectioned by FIB) showing the interface between neurons and USNWs. a) Sequential FIB sectioning showing the interface of neuronal soma and edge of USNW, b) Sequential FIB sectioning revealing first the tip of the USNW inside the soma, c) Sequential FIB sectioning revealing part of the USNW inside the soma and d) the whole USNW/neuron cross-section, full SEM image showing clear penetration of USNW electrode into the neuron soma, and e) cross-section showing multiple USNW penetrations into the cultured neurons.

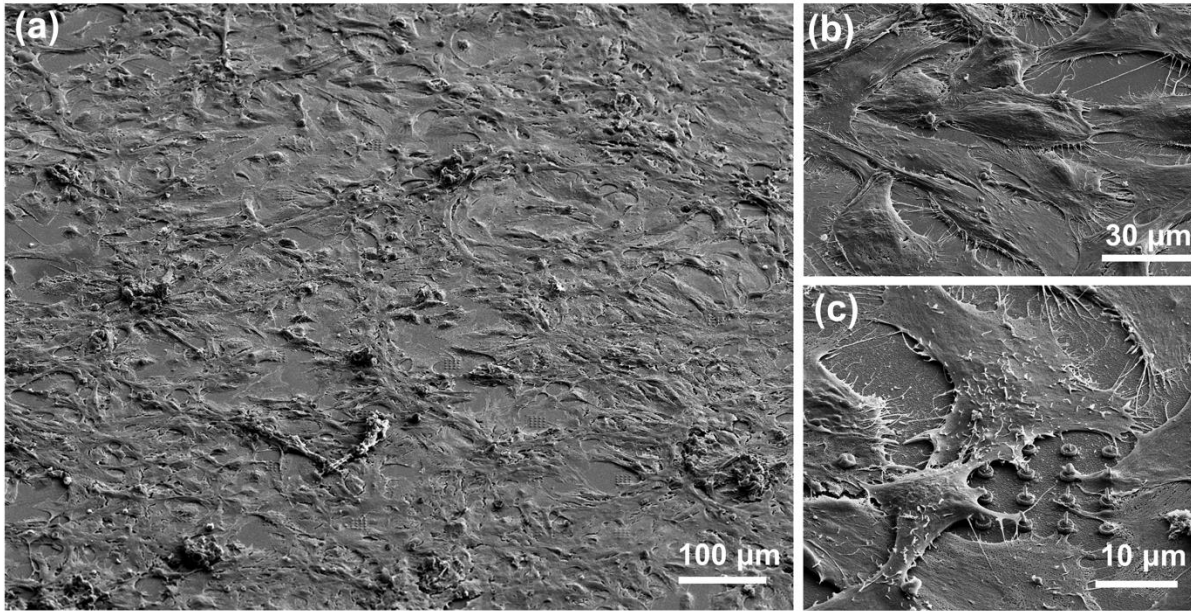


Figure S17. SEM images of cultured iPSC-CVPCs on the USNW platform: a) overview SEM image of the iPSC-CVPCs on the USNW arrays. b) Zoomed-in SEM image of the iPSC-CVPCs. c) Zoomed-in SEM image of iPSC-CVPCs on the USNW arrays.

5. Electrophysiological recordings of neuronal and cardiomyocyte activity

Multiple arrays with variable USNW pitches (5 μm , 10 μm , 30 μm , and 70 μm) were investigated where each array was composed of 32 USNWs. Electrophysiological recordings were carried out starting at 7 DIV for neurons (**Figure S18**) and at 5-7 DIV for iPSC-CVPCs (Figure S23 and Figure S24) using Intan RHS2000 stim/recording system. A Pt wire was used as the ground and reference electrodes, and a sampling rate of 30000 samples s^{-1} was used for the recording. The biphasic-pulse stimulation peak width, amplitude and frequency were 0.5 ms, 10 nA and 1 Hz, respectively. Matlab codes provided by Intan Technologies were used to convert raw data files into accessible format and post-processing.

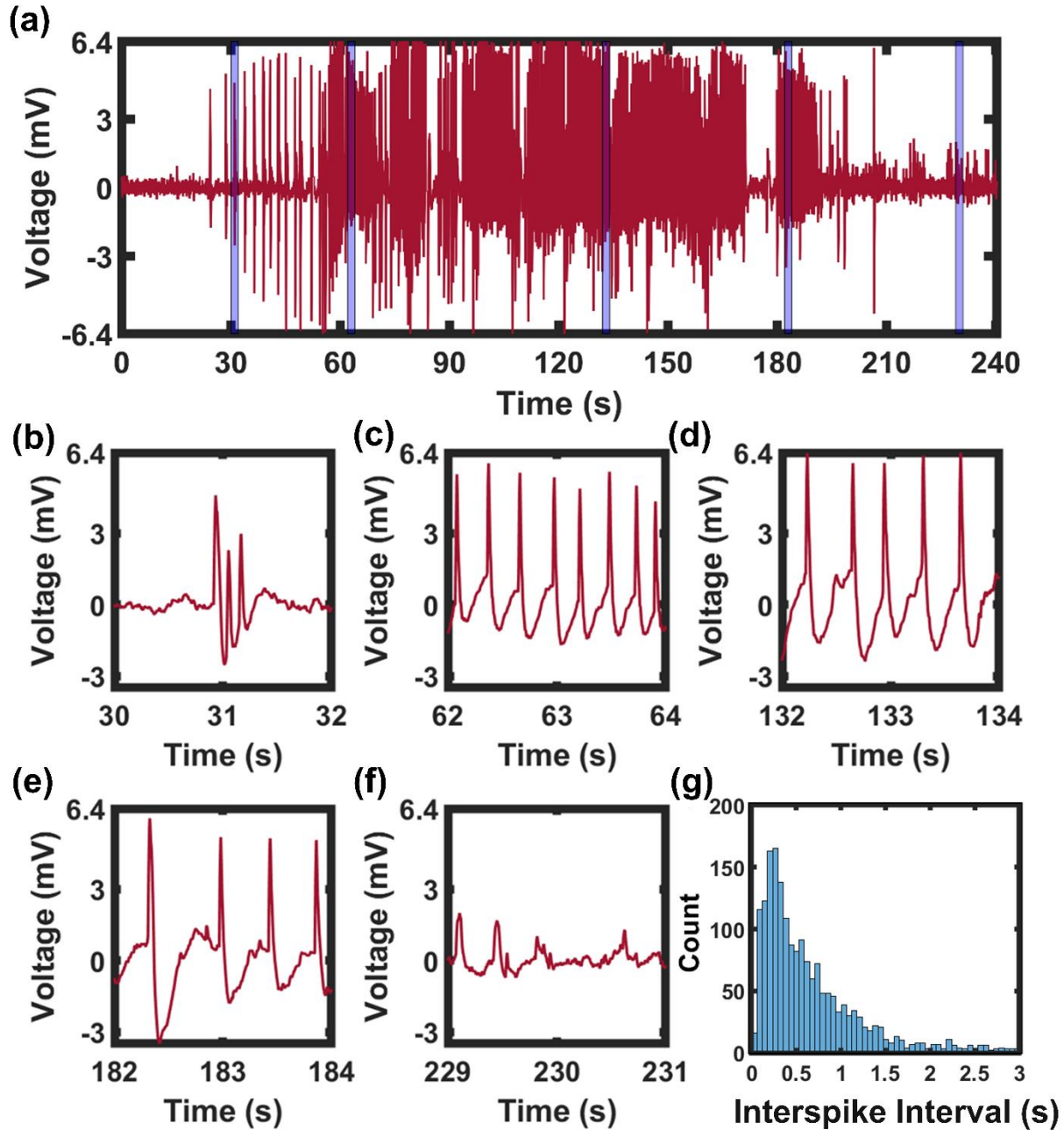


Figure S18. Single USNW recording segment demonstrating consistent signal amplitude over time and interspike analysis a) Continuous, 240 s recording segment from channel 31 USNW from group B (10 μm electrode spacing) at 11 DIV, showing consistent amplitude without attenuation. b-f) Close-up image of selected time segment over 240 s. The large amplitude action potential shapes c-e) throughout the recording duration remain consistent. g) The interspike interval width has an exponentially decaying tail, corresponding to action potential refractory periods and spike triggering from random processes.

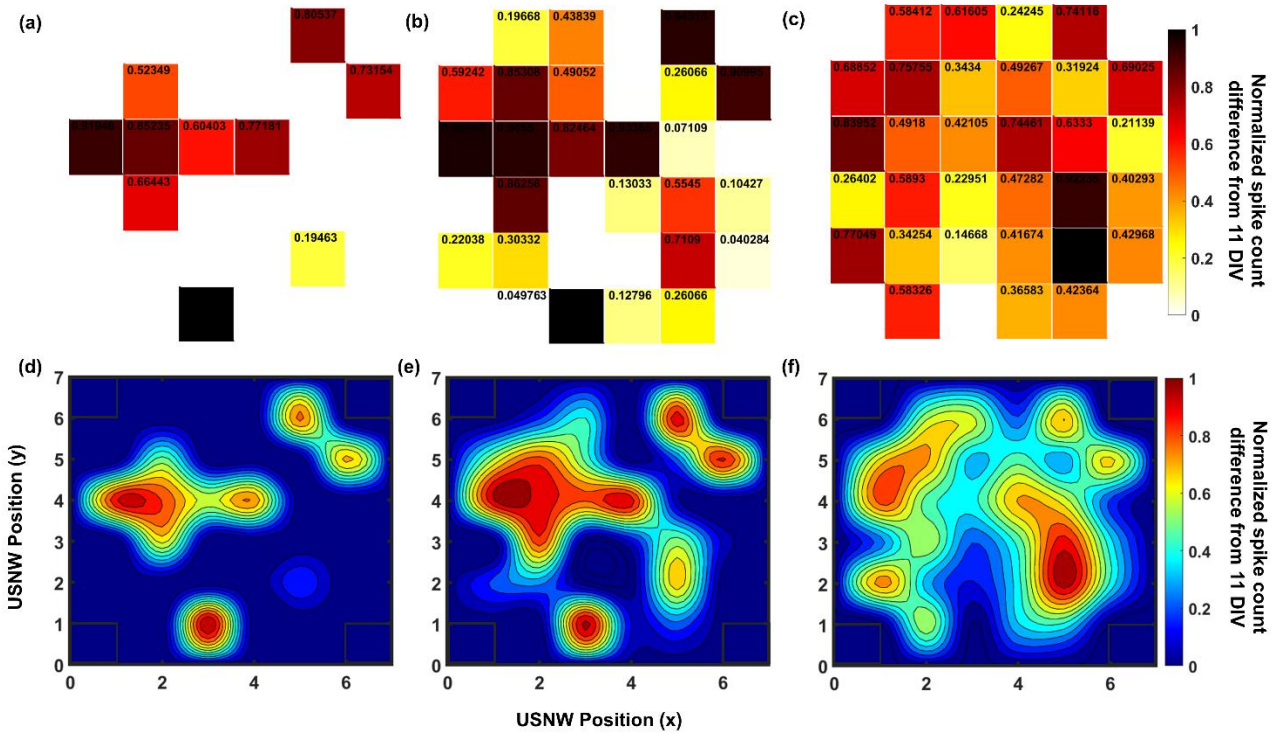


Figure S19. Normalized spike activity differences of USNW channels between 13, 15, and 19 DIV with 11 DIV. a) Normalized spike count difference from 11 DIV and 13 DIV (normalized to the maximum spike activity difference observed in the particular recording day across 32 channels). White square spaces indicate no increase in spike activities from 11 DIV. b) Normalized spike count difference from 11 DIV and 15 DIV. c) Normalized spike count difference from 11 DIV and 19 DIV. d-f) Contour map of normalized spike activity differences of 32 channels from 13, 15, and 19 DIV with spike activities from corresponding channels at 11 DIV, group B. The contour maps were plotted with 10 layers (10 channels with increased activity at 13 DIV from 11 DIV) and the 2D mesh grids were interpolated to provide more smooth contours. As the cells are cultured longer, we gradually see increase in spike activities across all 32 channels.

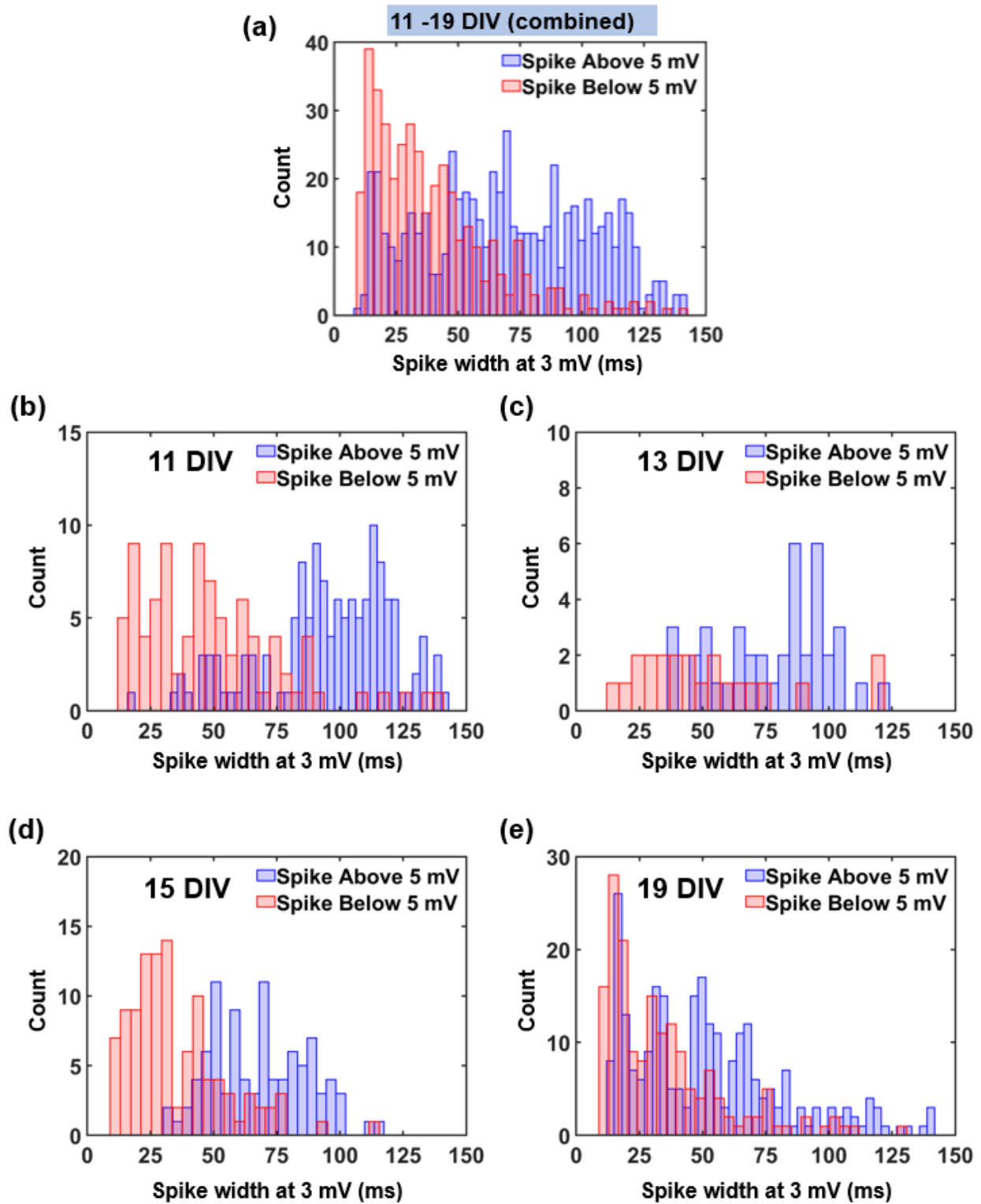


Figure S20. Histogram plot of spike width at 3 mV to compare spikes above and below 5 mV by days of culture. a) Combined histogram plot of spike width from 11 to 19 DIV. b) Histogram

plot of spike width at 11 DIV (~360 detected spikes above 5 mV, ~90 spikes below 5 mV). c) Histogram plot of spike width at 13 DIV (~40 detected spikes above 5 mV, ~20 spikes below 5 mV). d) Histogram plot of spike width at 15 DIV (~90 detected spikes above 5 mV, ~100 spikes below 5 mV). e) Histogram plot of spike width at 19 DIV (~520 detected spikes above 5 mV, ~170 spikes below 5 mV).

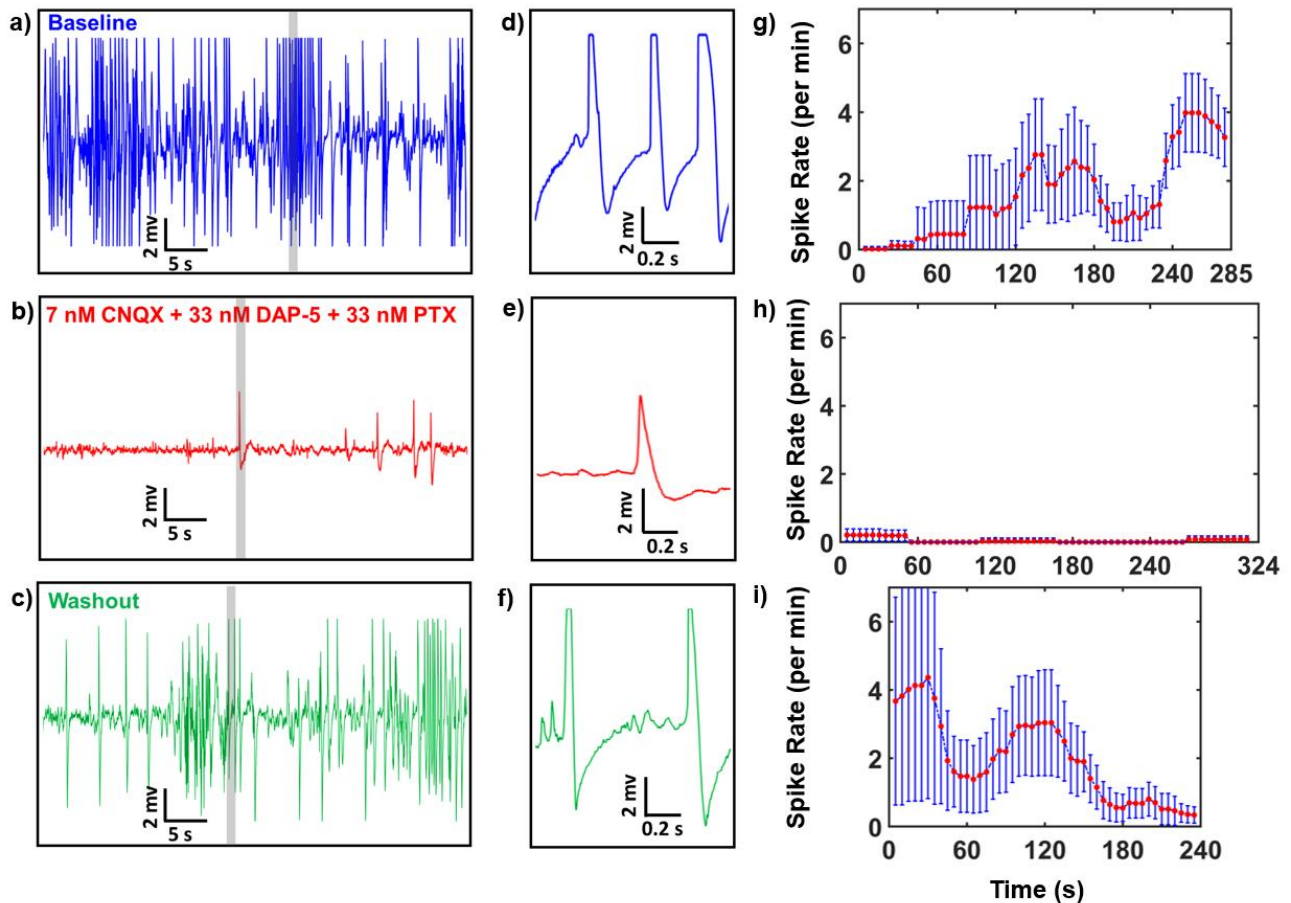


Figure S21. Example pharmacological interrogation at 8 DIV involving CNQX, DAP-5, and PTX to validate the pre-potentials. Expanded views the recording traces at the gray-highlighted regions are shown. a) 50 s baseline recording trace with action potential spikes. b) 50 s recording trace after addition of 7 nM CNQX, 33 nM DAP-5, and 33 nM PTX. c) 50 s recording trace after sequential washout. d) Zoomed-in 1 s segment of baseline recording. e) Zoomed-in 1 s recording segment after addition of 7 nM CNQX, 33 nM DAP-5, and 33 nM PTX. f) Zoomed-in 1 s recording segment after washout. g) Spike rate per min of baseline recording (285 s total) after high pass filtering h) Spike rate per min of recording after addition of 7 nM CNQX, 33 nM DAP-5, and 33 nM PTX (324 s total) after high pass filtering i) Spike rate per min of recording after washout (240 s total) after high pass filtering.

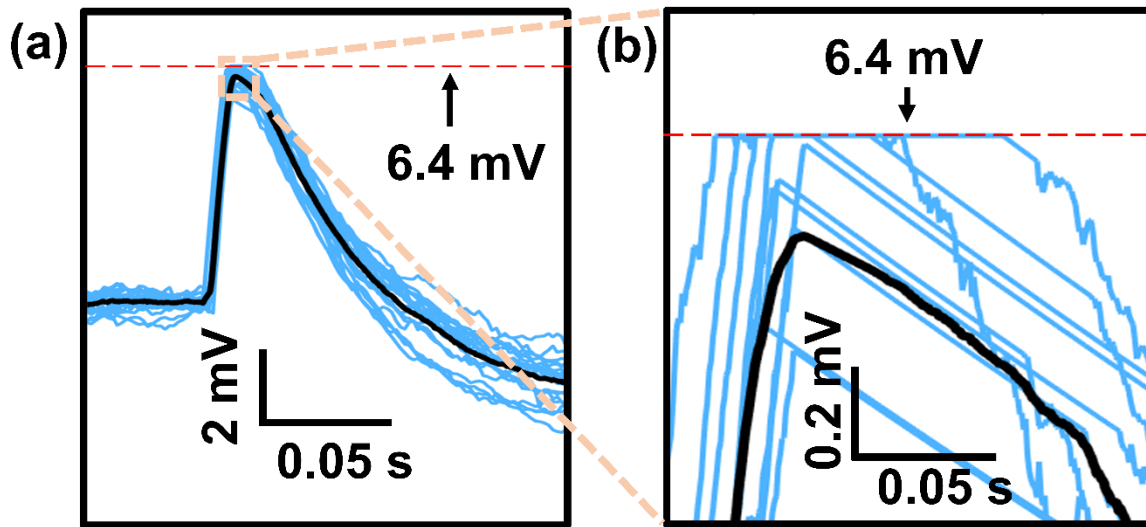


Figure S22. a-b) Selected time segment of the spike-sorting result shows clipping of recorded action potentials of *in vitro* iPSC-CVPCs at the Intan amplifier analog-to-digital converter (ADC) limit of ± 6.4 mV.

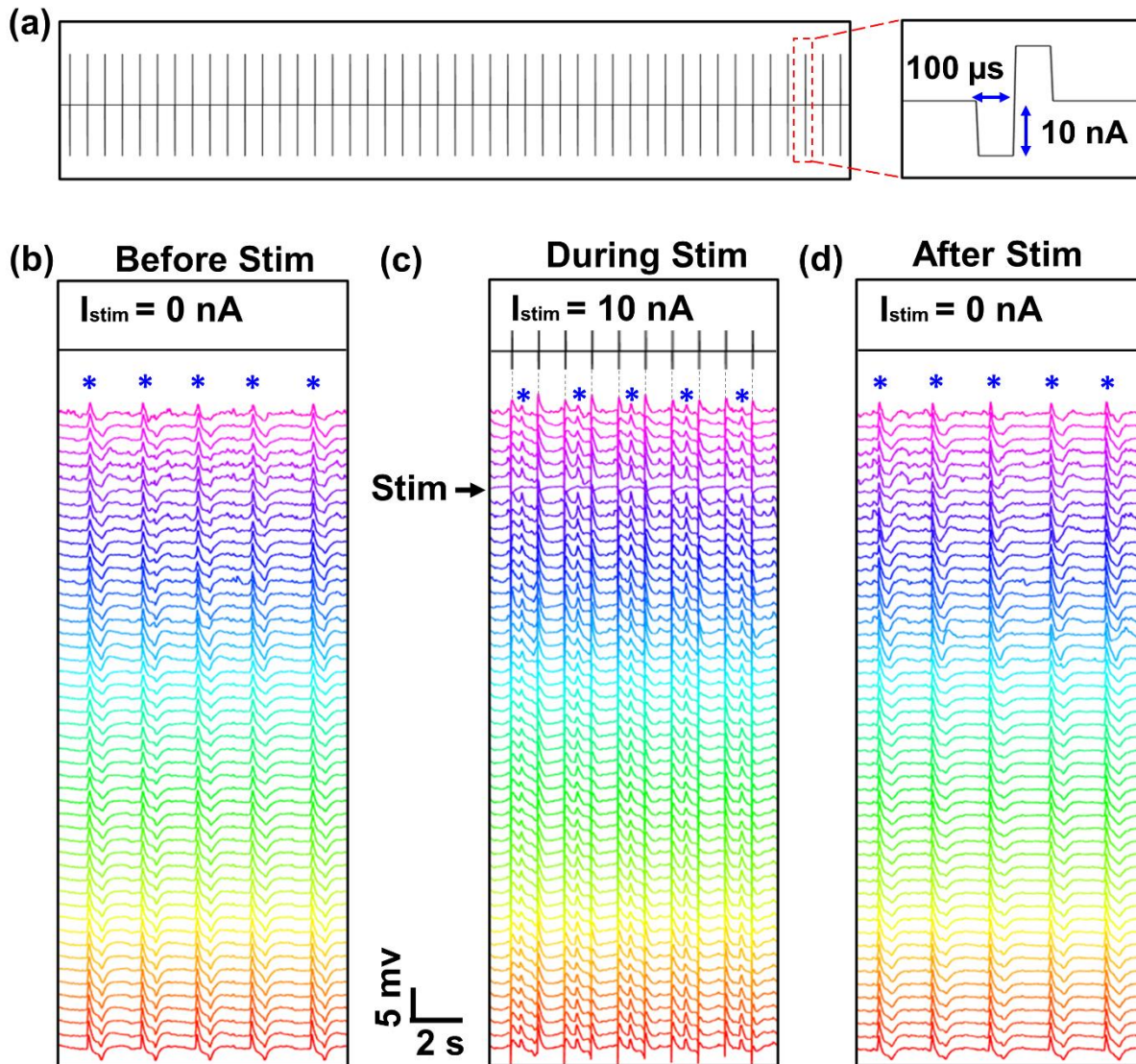


Figure S23. a) The biphasic-pulse stimulation traces with stimulation peak width, amplitude and frequency of 0.5 ms, 10 nA and 1 Hz, respectively. b) 52-Channel voltage traces of 2 arrays recorded from the iPSC-CVPCs at day 34 of differentiation before stimulation. c) 52-channel voltage traces of 2 arrays recorded from the iPSC-CVPCs at day 34 of differentiation during stimulation with the stimulation channel labeled in c). Gray dashed lines align the stimulation peaks with “artifact” spikes recorded from USNW electrodes due to capacitive coupling. d) 52-Channel voltage traces of 2 arrays recorded from the iPSC-CVPCs at day 34 of differentiation after stimulation. Action potential peaks are labeled as blue stars in b-d).

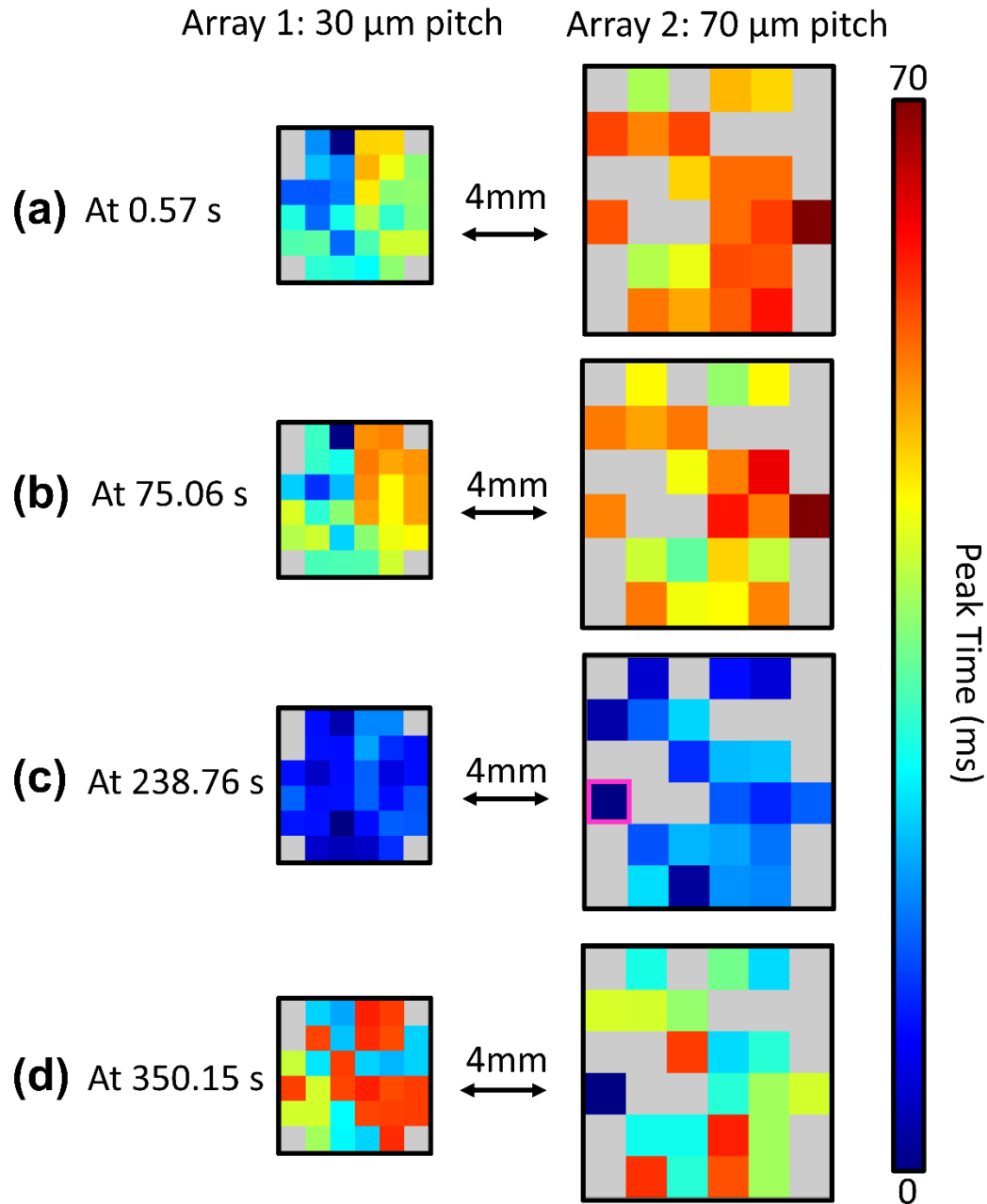


Figure S24. Mapping of action potential propagation patterns across the 2 arrays according to the array size scale at different time points before (a) at 0.57 s and b) at 75.06 s) and after (c) at 238.76 s and d) at 350.15 s) electrical stimulation. The distance between array 1 with 30 μm pitch and array 2 with 70 μm pitch was 4 mm. Two intracellular recordings before electrical stimulation (at 0.57 s and at 75.06 s) show action potential propagation from left to right, whereas intracellular recordings after electrical stimulation show an evolution from homogeneous firing at 238.76 s to a reserved propagation direction from right to left, where the action potential propagation direction starts from the stimulating electrode. The biphasic-pulse stimulation peak width, amplitude and frequency were 0.5 ms, 10 nA and 1 Hz, respectively. The stimulation channel location is shown as the pink box in c).

6. Channel selection, auto-thresholding spike sorting, and detected spike data analysis

6.1 Channel selection via cross-correlation matrix

For signal amplitude and spike sorting data analysis, observed channels and chosen USNW bank arrays were selected based on the USNW group and channels exhibiting largest amplitudes and displayed intracellular action potential waveforms upon visual inspection. For recording datasets with relatively low intracellular activities 11 DIV for single USNW, 11 to 19 DIV for 16 USNW and 625 USNW, channels and groups exhibiting low signal cross-correlation coefficient between one another (Figure S25i-k) to isolate channels with electrophysiological signals. The cross-correlation coefficient plot (Figure S25e-k) between each channel were determined based on sample 10 s data segments, with darker colors representing lower correlation. Figure S25e,f show cross-correlation plot of group B channels (from 11 to 19 DIV) and show evolution of neural networks over the culture time. Figure S25a-d show the corresponding longest segment from group B array for 11 to 19 DIV dataset. Primarily, group B array and few channels from group C array for 625 USNWs per channel sample that were incorporated into the signal amplitude analysis. For pharmacological analysis (at 7 DIV), single channel of USNWs were chosen and corresponding spike rates were calculated and observed.

Starting from 13 DIV, we observed strongly correlated activity across all channels within an individual array. The measured signals were essentially identical across majority of the channels (extremely similar spike counts as shown in Figure 3c,e) and showed strong inter-channel cross-correlation (Figure S25f,g). These most likely resulted since the time delay is too short to be detected because of the high density/tight pitch of our USNW electrodes for recording the signal propagation of the neurons in the network. According to the published result that the

propagation speed for *in vitro* neuronal network is 110 mm s^{-1} ,^[8] the time delay between two electrodes with $10 \text{ }\mu\text{m}$ spacing is less than 0.1 ms , which is nearly the limit for our recording temporal resolution.

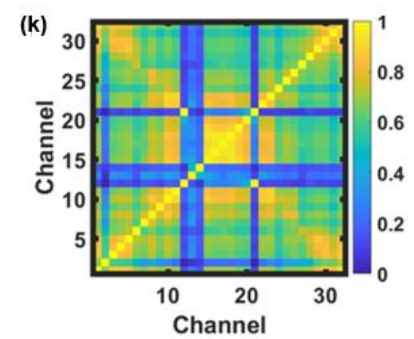
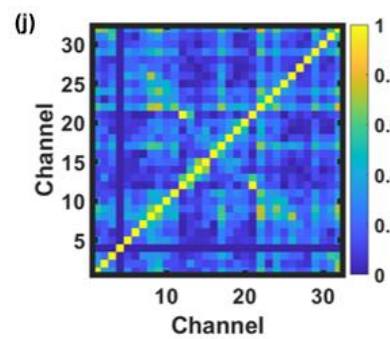
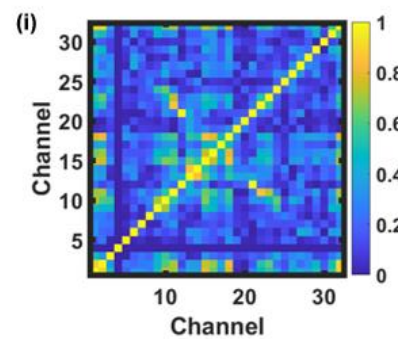
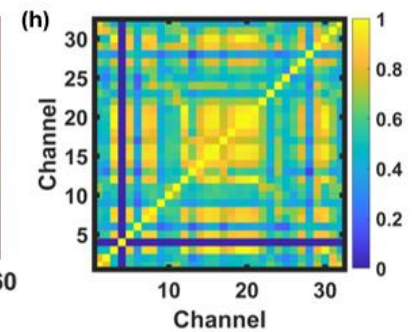
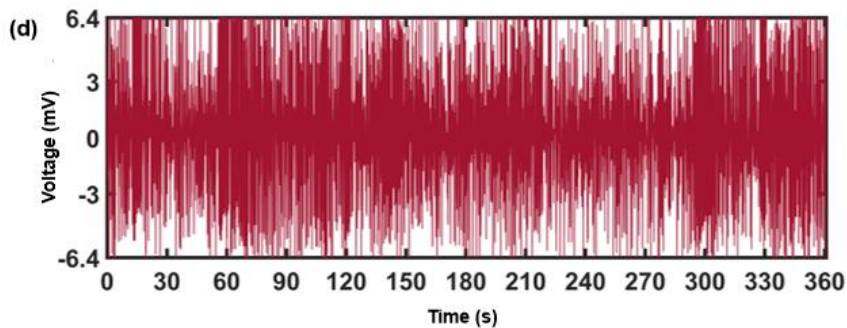
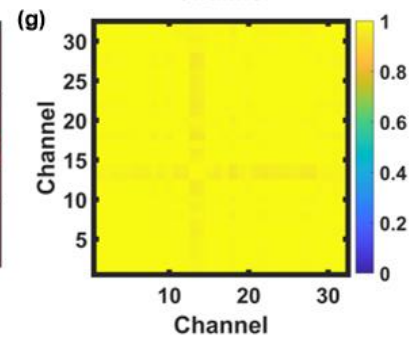
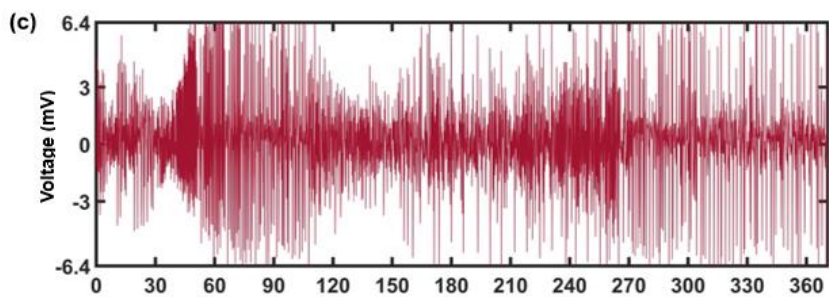
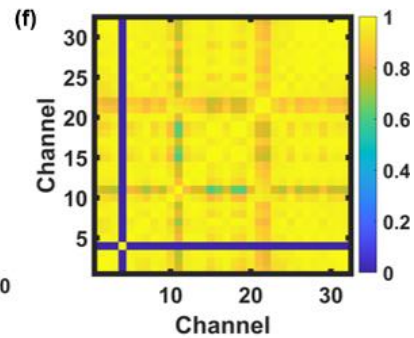
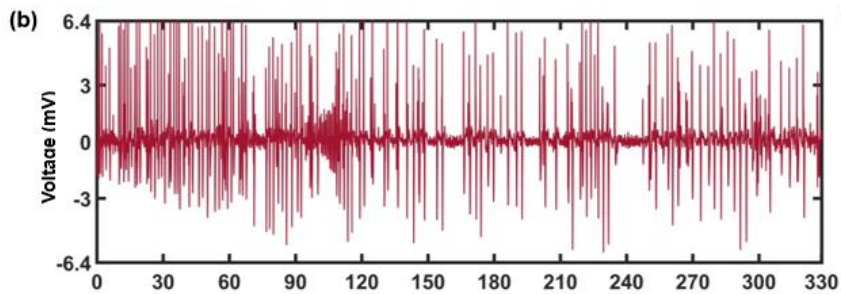
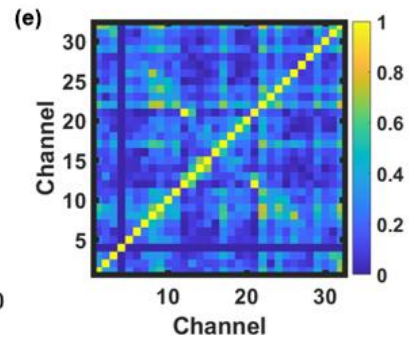
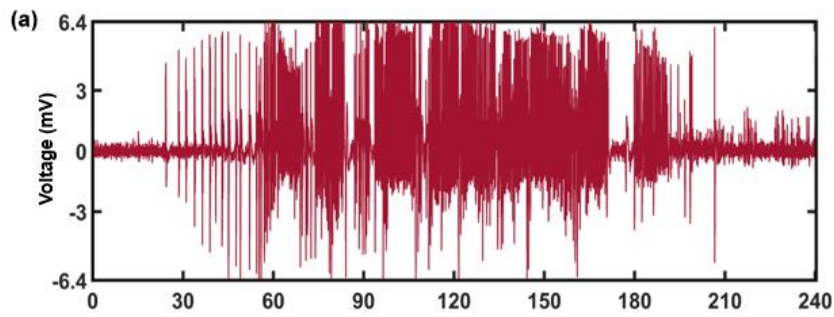


Figure S25. Longest single USNW recording segments 11-19 DIV and corresponding spike counts and spike rates a) Continuous, 240 s recording segment from channel 31 USNW from group B (10 μm electrode spacing) at 11 DIV (spike rate of 1.89 spikes s^{-1}). b) Continuous, 330 s recording segment from channel 31 USNW from group B at 13 DIV (mean spike rate of 0.45 spikes s^{-1} across 31 channels). c) Continuous, 370 s recording segment from channel 31 USNW from group B at 15 DIV (mean spike rate of 1.13 spikes s^{-1} across 32 channels). d) Continuous, 360 s recording segment from channel 31 USNW from group B at 19 DIV (mean spike rate of 2.52 spikes s^{-1} across 31 channels). e-h) Cross-correlation matrix for selected USNW groups for analysis from 11, 13, 15, and 19 DIV. e) Single USNW per channel, group B at 11 DIV. f) Single USNW per channel, group B at 13 DIV. g) Single USNW per channel, group B at 15 DIV. h) Single USNW per channel, group B at 19 DIV. The low cross-correlation correspond to large variance in spike counts observed for Figure 3g. i-k) Example cross-correlation matrix for selected USNW groups for analysis from batches at 11 DIV, i) 16 USNWs per channel, group B at 11 DIV, j) 625 USNWs per channel, group B at 11 DIV, k) 625 USNWs per channel, group C at 11 DIV.

6.2 Auto-threshold spike sorting

For spike sorting, selected channels for data analysis were high-pass filtered at 270 Hz for pharmacological experiments and unfiltered for signal amplitude comparison studies to retain the recorded peak-to-peak amplitude (to maximize the amplitude fidelity and perform more impartial comparison between pads driving different USNW counts). The positive and negative threshold values were determined and set for every selected channel with multiple of the normalized standard deviation, where our estimated thresholds were set to range from $4 - 6.5 \sigma_n$ ^[9] for high-pass filtered data and thresholds were set and ranged from 1 to $4 \sigma_n$ for unfiltered, raw data. After determining the positive and negative threshold values from the autothresholding algorithm for every selected channel, spike sorting was carried out for all channels with the respective threshold values against data segments recorded after biphasic current injection (data segment length of 180 s for pharmacology experiments and approximately 240 to 370 s for signal amplitude studies from recording segments at 11 to 19 DIV).

Spikes of both polarities, exceeding both positive and negative thresholds with temporal widths between 5 ms and 100 ms of each other (respectively considering the short spikelets and temporal broadening of potential spikes from the parasitic capacitance of the measurement system), were coupled as one spiking event to ensure intracellular action potentials were detected. Our spike detection begins when the signal initially exceeds the positive threshold. The local maximum is then determined between the time segment when the signal first exceeds and decreases back down to the set positive threshold again. From the local, positive maximum, if the spikes reached negative threshold within reasonable timeframe (within 100 ms) without the signal exceeding positive threshold for longer than 5 ms, then the local minimum is then determined between the time segment when the signal exceeds and reaches the set negative threshold again. Peak-to-peak amplitude is the magnitude difference between the local maximum and local minimum. Figure S26 shows an example segment of our spike detection method for unfiltered signal with the thresholds determined from the auto-threshold algorithm. By defining spikes to always contain positive and negative spike components alongside reasonable time duration between such two spikes, short, low-amplitude, and unipolar spikelets exceeding their corresponding positive or negative thresholds were automatically excluded out during the spike sorting.

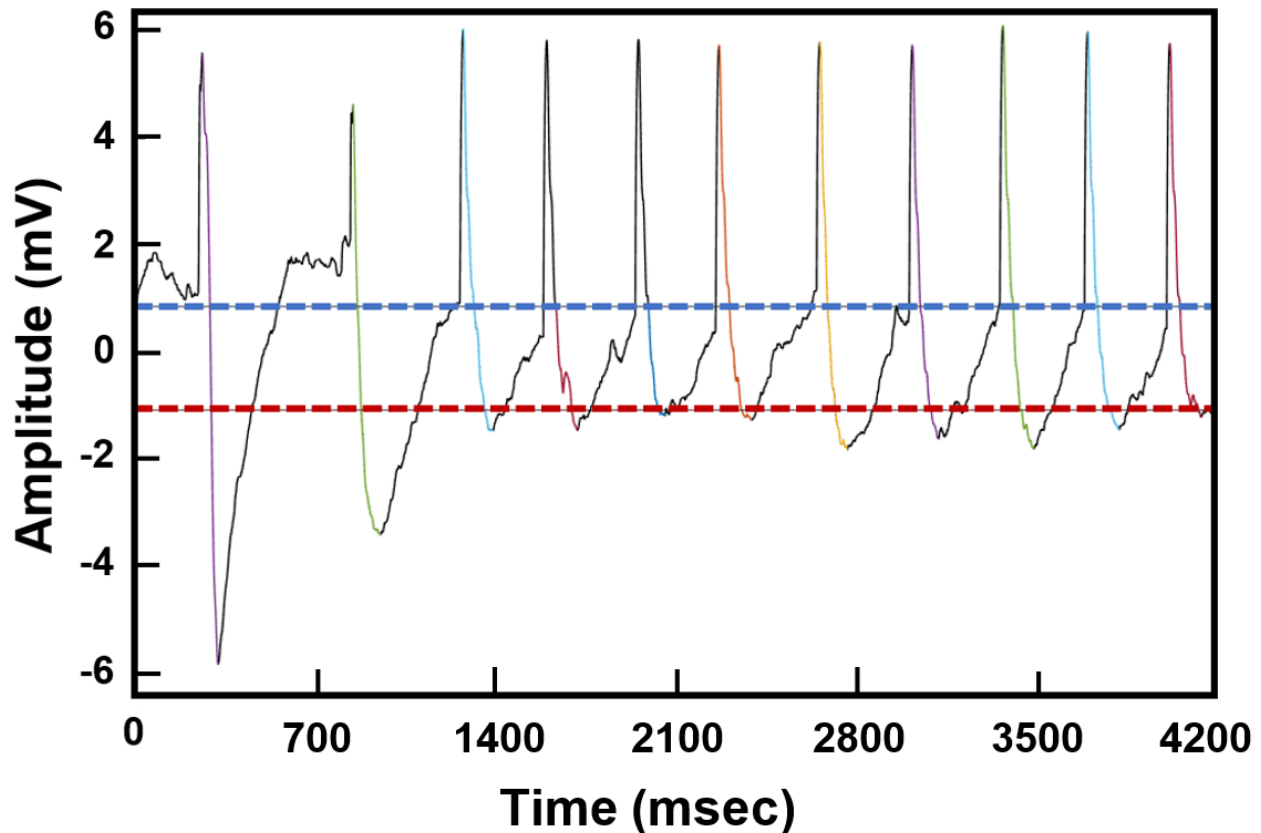


Figure S26. Auto-thresholding spike sorting example plot with positive and negative thresholds
a) Example of unfiltered signal and detected spikes with positive and negative thresholds (dashed blue and red lines respectively, thresholds are set at 1.6 and -1.6σ). Peak-to-peak amplitude is determined from local maxima and minima respectively above and below the thresholds, shown with varied colored lines.

6.3 Misc. data analysis from detected spikes

For spike rate analysis from 180 s time segment (Figure 3u-w) for baseline signal, signal after PTX application, and signal after TTX application, spike rates were calculated by determining the number of detected spikes every 5 s. With spike rate determined for every 5 s, 35 spike rate data points were plotted for selected channels over 180 s of recording. Channels exhibiting large, more than tenfold, deviation from the mean spike rate were excluded (ultimately, 27 channels were used to plot the spike rates for baseline signals, signals with PTX, and signals with TTX).

Interspike interval is determined by measuring the time between each positive, maximum peaks of the detected spikes, and the obtained interspike intervals are centered around 500 to 700 ms range (Figure S18g). The spike widths range near approximate mid-point of the recorded intracellular potentials range up to approximately 150 ms and were generally around 50 to 75 ms (Figure S20a), so the calculation of interspike interval based on the spikes' maximum peak point is a fair approximation.

7. Small Signal Circuit Modeling of Individually Addressable USNW versus Multi-USNWs per Channel

Building off of the circuit modeling of the electro-neural interface we performed previously,^[10] we simulated the effects of adding multiple NWs on a single recording channel. We started by adopting a typical patch-clamp measured sodium and potassium transmembrane current as a signal source, and building an appropriate RC network around this source. Figure 5h showed this small signal model for a single intracellular USNW penetrating a neural cell body. We modeled the excitable cell as having two lumped membrane impedances, one of which contains active ion channels that contribute to the generation of an action potential, denoted as a junctional membrane, and the other which is assumed to be a passive impedance modeling leakage from the inside of the cell to the outside of the cell, denoted as a non-junctional membrane. Simulations were carried out using CADENCE Spectre circuit simulator software, and values for membrane capacitance, ion channel conductance, and spreading resistance were all matched to achieve an intracellular potential waveform shown in Figure S27 below. The ground of this circuit model exists some distance away from the cell; thus there exists some non-zero electrical impedance between the outside of the cell and ground. We modeled this impedance as a spreading resistance (R_{spread}) of electrolytic solution, and thus, a non-zero potential can exist just outside of the cell during an action potential. Note that this is important

for simulations of extracellular or juxtacellular configurations where the NWs do not fully penetrate the cell membrane. Further, the electrochemical interface between the intracellular fluid and the intracellular USNW is modeled as a simple parallel RC circuit (R_{EC} , C_{EC}) which aims to capture both faradaic and capacitive electrochemical transduction processes, and the quality of the membrane seal around this penetrating electrode is modeled with a sealing resistance (R_{seal}). Finally, depending on the cell geometry, extracellular fluid conductance, and other factors, there may exist a signal pathway between the non-junctional extracellular region and the junctional extracellular region; we introduced here an isolation resistance (R_{iso}) which attempts to capture this effect.

(a)

Parameter	Value
Camp	5.5pF
Cec	1pF
Cmj	10fF
Cmnj	1fF
Cp	1pF
Rec	65Mohm
Riso	8kohm
Rmj	200Mohm
Rmnj	10Gohm
Rseal_extra	1kohm
Rseal_intra	10Gohm
Rspread	10kohm

(b)

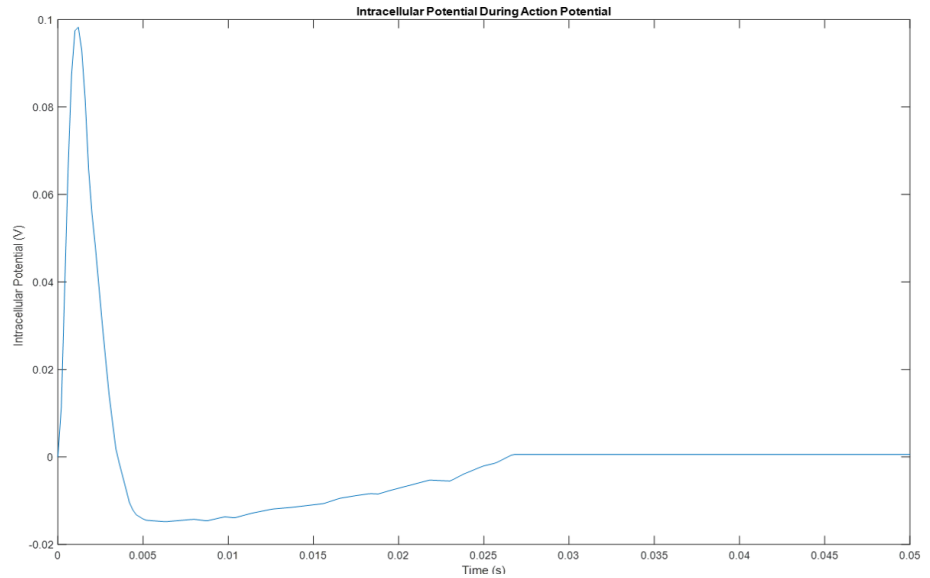


Figure S27. Default circuit parameters and corresponding simulated intracellular potential without any NW connected. The intracellular potential resulted from transmembrane currents taken from ^[10]. Cell circuit parameter values were tuned to achieve an intracellular to known amplitudes and spike durations of ~100mV peak with ~4 to 5 ms positive phase duration.

References

- [1] H. Z. Massoud, J. D. Plummer, E. A. Irene, *Journal of the Electrochemical Society* **1985**, 132, 1745.
- [2] M. Ganji, A. T. Elthakeb, A. Tanaka, V. Gilja, E. Halgren, S. A. Dayeh, *Advanced Functional Materials* **2017**, 27, 1703018.
- [3] T. Y. Chang, V. G. Yadav, S. De Leo, A. Mohedas, B. Rajalingam, C.-L. Chen, S. Selvarasah, M. R. Dokmeci, A. Khademhosseini, *Langmuir* **2007**, 23, 11718.
- [4] S. F. Cogan, *Annu. Rev. Biomed. Eng.* **2008**, 10, 275.
- [5] A. D'Antonio-Chronowska, M. K. Donovan, W. W. Y. Greenwald, J. P. Nguyen, K. Fujita, S. Hashem, H. Matsui, F. Soncin, M. Parast, M. C. Ward, *Stem cell reports* **2019**, 13, 924.
- [6] A. D'Antonio-Chronowska, M. D'Antonio, K. A. Frazer, *Bio-protocol* **2020**, 10, e3755.
- [7] J. Tønnesen, A. T. Sørensen, K. Deisseroth, C. Lundberg, M. Kokaia, *Proceedings of the National Academy of Sciences* **2009**, 106, 12162.
- [8] J. Abbott, T. Ye, K. Krenek, R. S. Gertner, S. Ban, Y. Kim, L. Qin, W. Wu, H. Park, D. Ham, *Nature biomedical engineering* **2020**, 4, 232.
- [9] J. M. Tanskanen, F. E. Kapucu, I. Vornanen, J. A. Hyttinen, presented at 2016 24th European Signal Processing Conference (EUSIPCO) **2016**.
- [10] R. Liu, R. Chen, A. T. Elthakeb, S. H. Lee, S. Hinckley, M. L. Khraiche, J. Scott, D. Pre, Y. Hwang, A. Tanaka, *Nano letters* **2017**, 17, 2757.